NATIONAL ADVISORY COMMITTEE FOR AERONAUTICS

REPORT 1337

DETERMINATION OF LONGITUDINAL STABILITY AND CONTROL CHARACTERISTICS FROM FREE-FLIGHT MODEL TESTS WITH RESULTS AT TRANSONIC SPEEDS FOR THREE AIRPLANE CONFIGURATIONS

By CLARENCE L. GILLIS and JESSE L. MITCHELL

1957

REPORT 1337

DETERMINATION OF LONGITUDINAL STABILITY AND CONTROL CHARACTERISTICS FROM FREE-FLIGHT MODEL TESTS WITH RESULTS AT TRANSONIC SPEEDS FOR THREE AIRPLANE CONFIGURATIONS

By CLARENCE L. GILLIS and JESSE L. MITCHELL

Langley Aeronautical Laboratory
Langley Field, Va.

National Advisory Committee for Aeronautics

Headquarters, 1512 H Street NW., Washington 25, D. C.

Created by Act of Congress approved March 3, 1915, for the supervision and direction of the scientific study of the problems of flight (U. S. Code, title 50, sec. 151). Its membership was increased from 12 to 15 by act approved March 2, 1929, and to 17 by act approved May 25, 1948. The members are appointed by the President and serve as such without compensation.

JAMES H. DOOLITTLE, Sc. D., Vice President, Shell Oil Company, *Chairman*

LEONARD CARMICHAEL, Ph. D., Secretary, Smithsonian Institution, *Vice Chairman*

ALLEN V. ASTIN, Ph. D., Director, National Bureau of Standards.

PRESTON R. BASSETT D. Sc.

DETLEV W. BRONK, Ph. D., President, Rockefeller Institute for Medical Research.

FREDERICK C. CRAWFORD, Sc. D., Chairman of the Board, Thompson Products, Inc.

WILLIAM V. DAVIS, JR., Vice Admiral, United States Navy, Deputy Chief of Naval Operations (Air).

PAUL D. FOOTE, Ph. D., Assistant Secretary of Defense, Research and Engineering. (Appointed member of Committee Oct. 22, 1957.)

WELLINGTON T. HINES, Rear Admiral, United States Navy, Assistant Chief for Procurement, Bureau of Aeronautics.

JEROME C. HUNSAKER, Sc. D., Massachusetts Institute of Technology.

CHARLES J. MCCARTHY, S. B., Chairman of the Board, Chance Vought Aircraft, Inc.

DONALD L. PUTT, Lieutenant General, United States Air Force, Deputy Chief of Staff, Development.

JAMES T. PYLE, A. B., Administrator of Civil Aeronautics.

FRANCIS W. REICHELDERFER, Sc. D., Chief, United States Weather Bureau.

EDWARD V. RICKENBACKER, Sc. D., Chairman of the Board, Eastern Air Lines, Inc.

LOUIS S. ROTHSCHILD, Ph. B., Under Secretary of Commerce for Transportation.

THOMAS D. WHITE, General, United States Air Force, Chief of Staff.

HUGH L. DRYDEN, PH. D., *Director*

JOHN W. CROWLEY, JR., B. S., *Associate Director for Research*

JOHN F. VICTORY, LL. D., *Executive Secretary*

EDWARD H. CHAMBERLIN, *Executive Officer*

HENRY J. E. REID, D. Eng., Director, Langley Aeronautical Laboratory, Langley Field, Va.

SMITH J. DEFRANCE, D. Eng., Director, Ames Aeronautical Laboratory, Moffett Field, Calif.

EDWARD R. SHARP, Sc. D., Director, Lewis Flight Propulsion Laboratory, Cleveland, Ohio

WALTER C. WILLIAMS, B. S., Chief, High-Speed Flight Station, Edwards, Calif.

REPORT 1337

DETERMINATION OF LONGITUDINAL STABILITY AND CONTROL CHARACTERISTICS FROM FREE-FLIGHT MODEL TESTS WITH RESULTS AT TRANSONIC SPEEDS FOR THREE AIRPLANE CONFIGURATIONS

By Clarence L. Gillis and Jesse L. Mitchell

SUMMARY

A test technique and data analysis method has been developed for determining the longitudinal aerodynamic characteristics from free-flight tests of rocket-propelled models. The technique makes use of accelerometers and an angle-of-attack indicator to permit instantaneous measurements of lift, drag, and pitching moments. The data, obtained during transient oscillations resulting from control-surface disturbances, are analyzed by essentially nonlinear direct methods (such as cross plots of the variation of lift coefficient with angle of attack) and by linear indirect methods by using the equations of motion for a transient oscillation.

The analysis procedure has been set forth in some detail and the feasibility of the method has been demonstrated by data measured through the transonic speed range on several airplane configurations. Where comparisons were possible, values of aerodynamic parameters determined by different methods showed generally very good agreement. In addition, it was shown that the flight conditions and dynamic similitude factors for the tests described were reasonably close to typical full-scale airplane conditions.

INTRODUCTION

Aerodynamic testing by means of free-flight techniques offers several obvious advantages; thus, considerable development of suitable test and analysis methods has been made by many organizations. Free-flight techniques embrace a wide range of vehicle sizes from small gun-launched projectiles to full-scale airplanes. The technique described herein was developed for the purpose of permitting investigations of the longitudinal stability, control, and performance characteristics of aircraft by means of rocket-propelled models of fairly large size.

Reference 1 contains a partial description of the technique for longitudinal stability and control measurements on free-flight models. The purpose of the present report which is based on references 2 to 4 is to describe the test procedure and to present a more comprehensive discussion of the method of analysis as it has been developed from a large number of model flight tests. For illustrative purposes, data are presented for three airplane configurations at transonic speeds. The model flight tests were performed at the Langley Pilotless Aircraft Research Station at Wallops Island, Va.

SYMBOLS

The axes system used is shown in figure 1.

a_n normal accelerometer reading, g units

a_l longitudinal accelerometer reading, g units

a_t transverse accelerometer reading, g units

A aspect ratio, b^2/S

a logarithmic damping constant

b wing span, ft

$C_{1/2}$ cycles to damp to one half amplitude
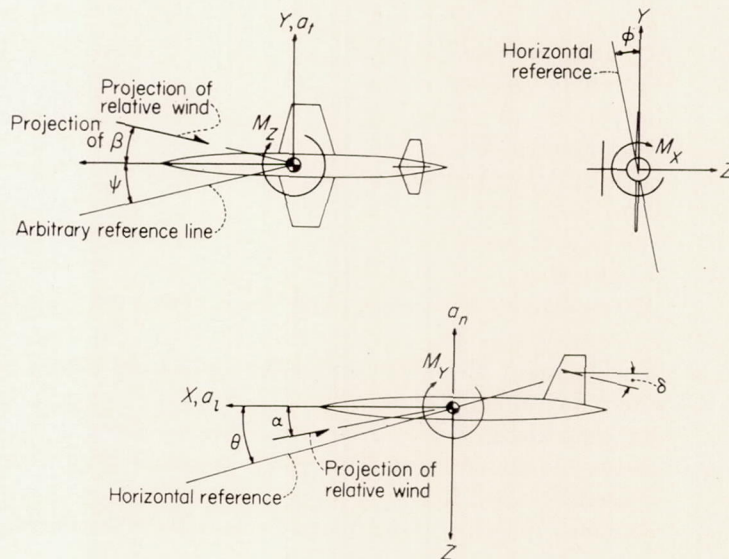
C_c chord force coefficient

FIGURE 1.—System of axes. Each view presents a plane of the axes system viewed along the positive direction of the third. Angular displacements as shown are positive.

C_D drag coefficient

C_L lift coefficient

C_N normal-force coefficient

C_m pitching-moment coefficient

c chord, ft

$\bar{c}$ mean aerodynamic chord, $\dfrac{1}{S}\displaystyle\int_{-b/2}^{b/2} c^2 dy$, ft

c_l section lift coefficient

D drag, lb

d length of cylindrical section of fuselage, in.

g acceleration due to gravity, 32.2 ft/sec^2

I_Y moment of inertia about Y-axis, slug-ft^2

$I'=\dfrac{I_Y}{qS\bar{c}}$

K drag-due-to-lift constant

K' constant used in aeroelasticity analysis

k_Y radius of gyration about Y-axis, ft

L lift, lb

l longitudinal distance between two normal accelerometers, ft

l_t tail length (distance from center of gravity to aerodynamic center of tail), ft

M Mach number

M_X moment about X-axis, ft-lb

M_Y moment about Y-axis, ft-lb

M_Z moment about Z-axis, ft-lb

m mass, slugs

$m'=\dfrac{mV}{qS}$

N normal force, lb

P period of oscillation, sec

p calibrated static pressure, lb/sq ft

p_∞ free-stream static pressure, lb/sq ft

p_o standard sea-level static pressure, 2116 lb/sq ft

$Q=qC_{L_{\alpha,r,w}}$

q dynamic pressure, lb/sq ft

R Reynolds number

r radius, in.

S wing area, sq ft

$T_{1/2}$ time to damp to one-half amplitude, sec

t time, sec

V velocity, ft/sec

W weight, lb

x_a displacement of accelerometer from center of gravity along X-axis, ft

x' displacement of air-flow indicator vane from center of gravity along X-axis, ft

x distance along X-axis from any reference point, ft

y_a displacement of accelerometer from center of gravity along Y-axis, ft

y spanwise distance along Y-axis from plane of symmetry, ft

y' spanwise distance along Y-axis from fuselage side, ft

y'_{cp} spanwise position of center of pressure of exposed semispan, ft

z_a displacement of accelerometer from center of gravity along Z-axis, ft

α angle of attack, deg or radians

α_{L0} angle of attack at zero lift

β angle of sideslip, deg

γ flight-path angle, radians

δ stabilizer deflection, deg or radians

ϵ downwash angle, radians

$\eta=\dfrac{y}{b/2}$

θ angle of pitch in equations of motion, radians; wing twist angle in plane parallel to plane of symmetry in aeroelastic analysis, radians

Λ sweepback angle, deg

μ relative density factor, $m/\rho S\bar{c}$

ρ atmospheric density, slugs/cu ft

φ roll angle, radians

ψ yaw angle, radians

Ω phase angle, radians

ω frequency of pitch oscillation, sec^{-1}

Subscripts:

cg at center of gravity

$nose$ at model nose

i indicated

ac aerodynamic center

t trim, when used with α and C_L

T total

r rigid

e elastic

0 at zero α and δ

min minimum

a accelerometer location

$aero$ aerodynamic

b wing normal-force balance

w exposed wing

av average

A single dot over a symbol indicates the first derivative with respect to time; a double dot indicates the second derivative with respect to time. The symbols α, δ, and C_L used as subscripts indicate the partial derivative of the quantity with respect to the subscript, such as

$$C_{L_\alpha}=\frac{\partial C_L}{\partial \alpha}$$

whereas the symbols $\dot\alpha$ and q used as subscripts represent the partial derivative of the quantity with respect to the nondimensional quantities $\dfrac{\bar{c}}{2V}$ and $\dfrac{\dot\theta\bar{c}}{2V}$, respectively, such as

$$C_{m_q}=\frac{\partial C_m}{\partial\left(\dfrac{\dot\theta\bar{c}}{2V}\right)}$$

TEST PROCEDURE

The rocket-propelled models are launched from the ground and are propelled by solid-fuel rockets. Information on the

steady-state and transient motions of the models is obtained by applying intermittent disturbances, by means of a control-surface deflection, for example, and recording the resulting motions. These motions are measured by internal instrumentation in the models and are transmitted by telemeter to ground receiving stations. Flight-path information is obtained by means of ground-based radar techniques. Data reduction and analysis of the telemeter and radar records yields data on the lift, drag, and pitching-moment characteristics of the models. Continuously recording equipment is used to permit the detection of rapid changes in the measured quantities.

MODELS

The four models used for illustrative purposes in the present investigation were part of a general research study of the effects of wing plan form on the transonic aerodynamic characteristics of airplane configurations. Sketches of the models are shown in figure 2 and photographs, in figure 3. The models included three wing plan forms: unswept, 45° sweptback, and 60° delta. The geometric characteristics of the various wings are given in table I. One model of each configuration was constructed with a solid-steel wing and an additional model of the swept-wing configuration was constructed of solid duralumin to permit measurement of aeroelastic effects.

The fuselages were bodies of revolution having cylindrical center sections. The nose and tail sections were defined by the ordinates of table II. The fuselages were composed of five separable sections constructed of sheetmetal skin attached to connecting rings. The vertical-tail surfaces were of constant thickness and had wedge leading and trailing edges. The vertical tails were constructed of wood and plastic and had aluminum surface inlays.

The solid-aluminum horizontal tails were the same for all models and had plan forms and airfoil sections identical to those of the unswept wing. The horizontal tails were mounted on ball bearings built into the vertical tails (fig. 4) and were pivoted about a hinge line at 42 percent of the tail mean aerodynamic chord. For the swept-wing models the gaps at the roots of the horizontal tails were sealed by means of wiper-type seals. For the other two models these gaps were left unsealed. In order to produce the longitudinal motions of the models during flight, the horizontal-tail surfaces were operated by control-actuating mechanisms in the rear sections of the fuselages. For the unswept-wing model this mechanism consisted of a cam operated by an electric motor. In the other three models this mechanism consisted of hydraulic power systems programed by means of electric motors. The control systems produced approximate square-wave motions of the horizontal tails. In both systems the time intervals of the control motions were preset by adjusting the speed of the electric motors.

The swept-wing and delta-wing models were equipped with an extra vertical tail below the fuselage as indicated in figure 2. This tail was geometrically identical to the upper
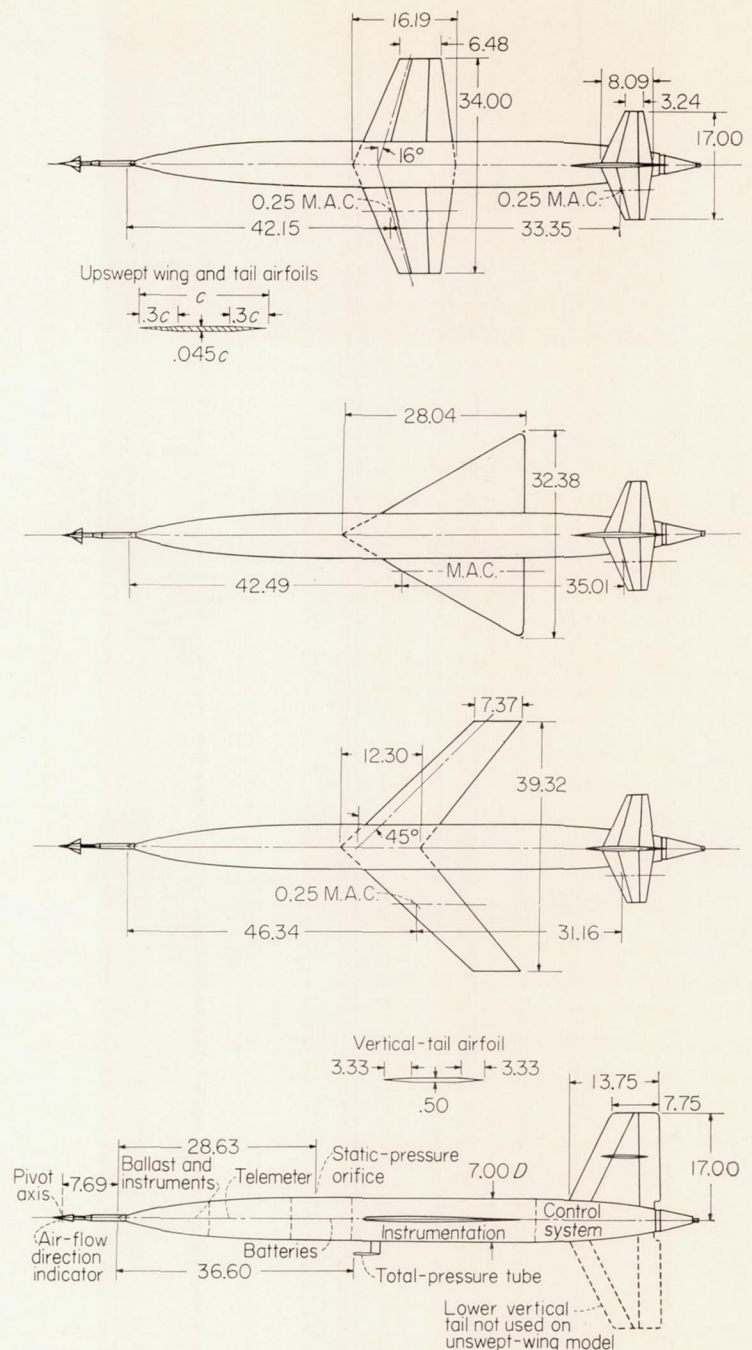

FIGURE 2.—General arrangement of models. All dimensions in inches.

vertical tail and was included on the models to minimize the possibility of lateral motions which had been encountered on other model flights.

INSTRUMENTATION

All models contained NACA telemeters which provided continuous records of the measurements of the internal instrumentation. The telemeter was located in the nose of the model and the transmitting antenna consisted of a wire imbedded in the leading edge of the vertical tail. Measurements made on all the models included normal and longitudinal acceleration near the model center of gravity, angle of
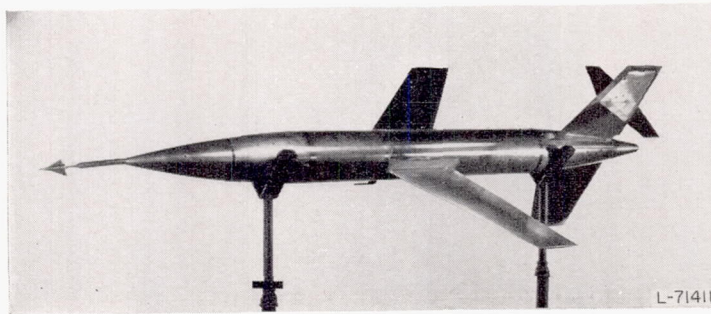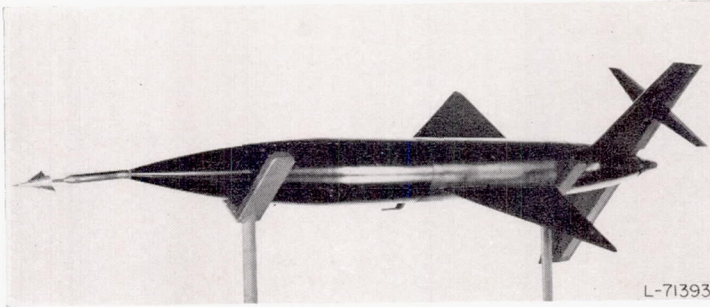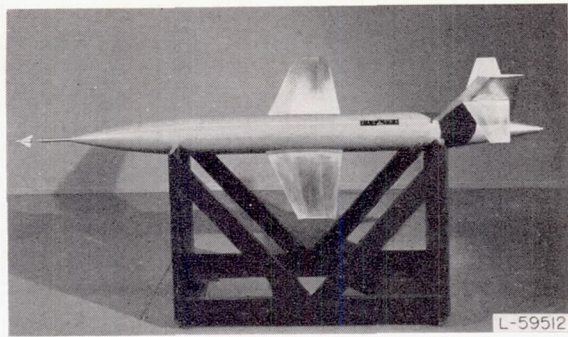
FIGURE 3.—Photographs of the three configurations.

TABLE I
WING GEOMETRY

	Unswept	Swept	Delta
Aspect ratio_____	3. 00	4. 00	2. 31
Taper ratio_____	0. 40	0. 60	0
Area (including fuselage), sq ft_	2. 68	2. 68	3. 15
Airfoil section (free-stream)__	Hexagonal	NACA 65A006	NACA 65A003
Thickness_____	0. 045c	0. 06c	0. 03c
Mean aerodynamic chord, in..	12. 03	10. 00	18. 70

attack, horizontal-tail deflection, total pressure, and a calibrated static pressure. On the swept- and delta-wing models, measurements were made of transverse acceleration and wing normal force. In addition, the measurements for the delta-wing and flexible swept-wing models included a measurement of normal acceleration in the nose, which in conjunction with the normal acceleration at the center of gravity provided a measure of pitching angular acceleration. A general view of the telemeter installation and instrumentation

TABLE II
FUSELAGE NOSE AND TAIL ORDINATES
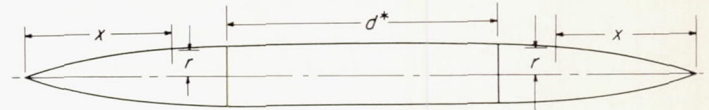
x, in.	r, in.
0	0. 168
0. 060	. 182
. 122	. 210
. 245	. 224
. 480	. 294
. 735	. 350
1. 225	. 462
2. 000	. 639
2. 450	. 735
4. 800	1. 245
7. 350	1. 721
8. 000	1. 849
9. 800	2. 155
12. 250	2. 505
13. 125	2. 608
14. 375	2. 747
14. 700	2. 785
17. 150	3. 010
19. 600	3. 220
22. 050	3. 385
24. 500	3. 500

*$d=40.00$ in. for unswept-wing model; $d=42.00$ in. for all other models.

in a typical model is shown in figure 5 and a more detailed view inside the model center section is shown in figure 6.

Angle of attack was measured by a free-floating vane-type instrument located ahead of the model nose. This instrument is more fully described in reference 5. The total range of this instrument is approximately ±15°. In order to permit measurements to somewhat higher positive angles of attack, the sting to which the vane was attached was mounted at a negative angle, with respect to the fuselage center line, of 6° for the delta-wing model and 5° for the flexible swept-wing model.

The total pressure was measured by a tube located under the fuselage (figs. 2 and 3) and the static pressure was measured at an orifice located on the top center line of the body at a station about 0.6 body diameters back of the beginning of the cylindrical section. Previous to the flight tests of the models described herein, a special instrumentation test model was flown to calibrate these pressure-measuring locations. This calibration model (fig. 7) was composed of the forward portion of the fuselage of the airplane models with an angle-of-attack vane, total- and static-pressure orifices, and a longitudinal accelerometer, mounted on a two-stage rocket-propelled test vehicle. Results from this test indicated that, within the accuracy of the measurements, the underslung total-pressure tube on this fuselage measured free-stream total pressure at small angles of attack up to at least $M=2.1$.
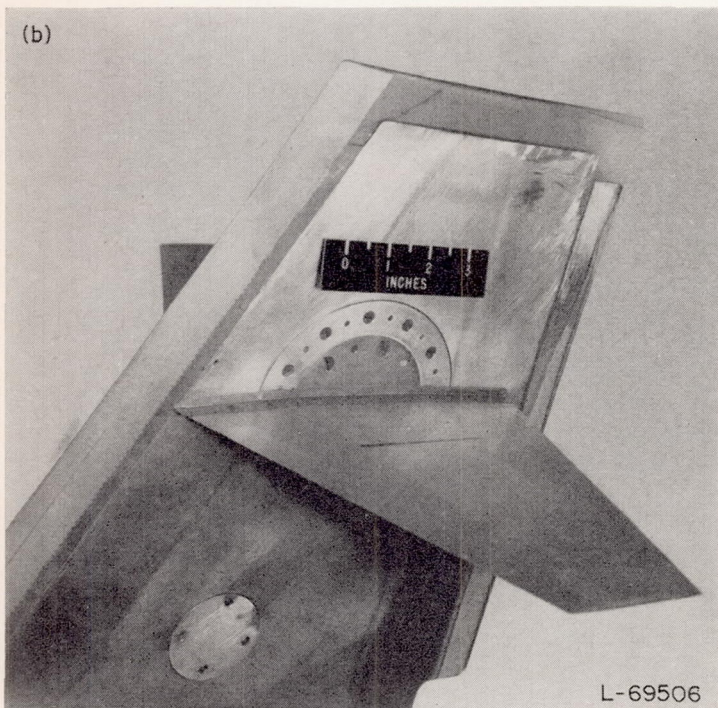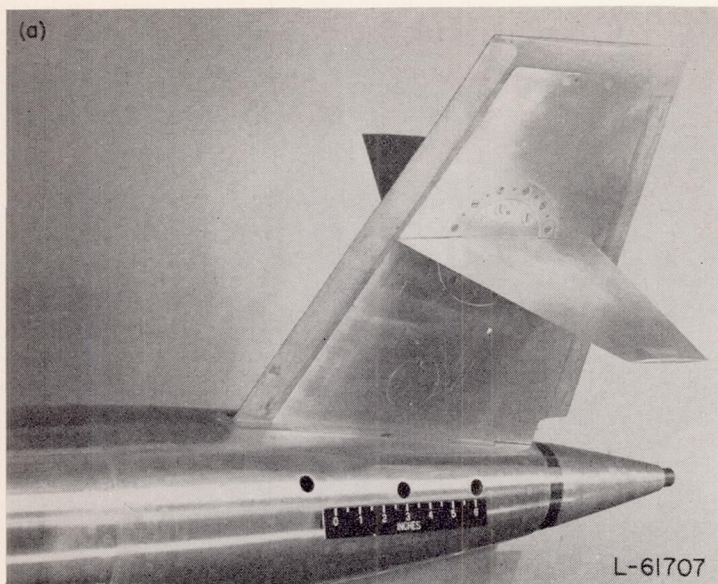
(a) Unsealed gap.
(b) Sealed gap.

FIGURE 4.—Empennage arrangement.

The calibration of the static-pressure orifice from the instrumentation test model is shown in figure 8. The static-pressure position error at supersonic speeds is small and relatively constant. The most important feature of the calibration curve in figure 8 is the sharp change in the pressure at a Mach number between 0.97 and 0.98. Many subsequent checks of this pressure variation on other models having the same fuselage indicate that, within the accuracy of measure-

ment, the sharp break always occurs at the same Mach number. Thus, when this pressure break appears on the flight time history, the Mach number can be established at that point irrespective of the absolute accuracy of the pressure measurements.

Wing normal force was measured by mounting the wing on a beam-type balance. (See fig. 9.) The balance was designed to permit vertical translation of the wing with respect to the bulkhead without angular motion. This vertical motion was measured by an inductance gage calibrated to give measurements of wing normal force. On the delta-wing model a strain gage was also attached to the wing-balance to furnish a duplicate measurement. The wing and balance assembly were fastened to the fuselage at the bulkhead. The gaps around the wing root where it entered the fuselage were sealed with rubber tubing or fabric.

Ground-based instrumentation was also utilized during the model flights. A CW Doppler radar unit was used to measure model velocity and a modified SCR 584 radar unit was used to obtain model position in space. An approximate measure of model rolling velocity was obtained from spinsonde radio receiving equipment (ref. 6) which recorded the rolling rate of the telemeter antenna radiation pattern. Atmospheric conditions for the model flights were obtained from standard radiosondes released immediately after each flight. Fixed and manually operated 16-millimeter motion-picture cameras were used to record the launching and initial portion of each flight.

PREFLIGHT MEASUREMENTS

The model flights described herein took place at low altitudes, the portions useful for data analysis occurring at less than 10,000 feet. The resulting high dynamic pressures introduced the possibility of aeroelastic effects. Estimations based on static loading tests and calculations indicated that for the unswept and delta wings the aerodynamic effects of elasticity were negligible. For the swept wings, however, the effects were appreciable. Shown in figure 10 are the structural influence coefficients determined from static loading tests of the duralumin swept wing. The coefficients are shown as the twist in the free-stream direction per unit load applied at various spanwise stations along the 25- and 50-percent chord lines.

For use in analyzing any flutter or buffeting vibrations that occurred in flight, the vibration frequencies of the model components were determined by suspending the models in shock cords and vibrating by means of an electromagnetic shaker and by striking the wings and fuselages. The resonant frequencies were determined by visual observation and from the records obtained from the model instrumentation and telemeter during the vibration tests.

After installation of all instrumentation, the weight, center of gravity, and moments of inertia of each model were measured. These quantities are given in table III. Moments of inertia were determined by swinging the models as pendulums and recording the frequency of oscillation.
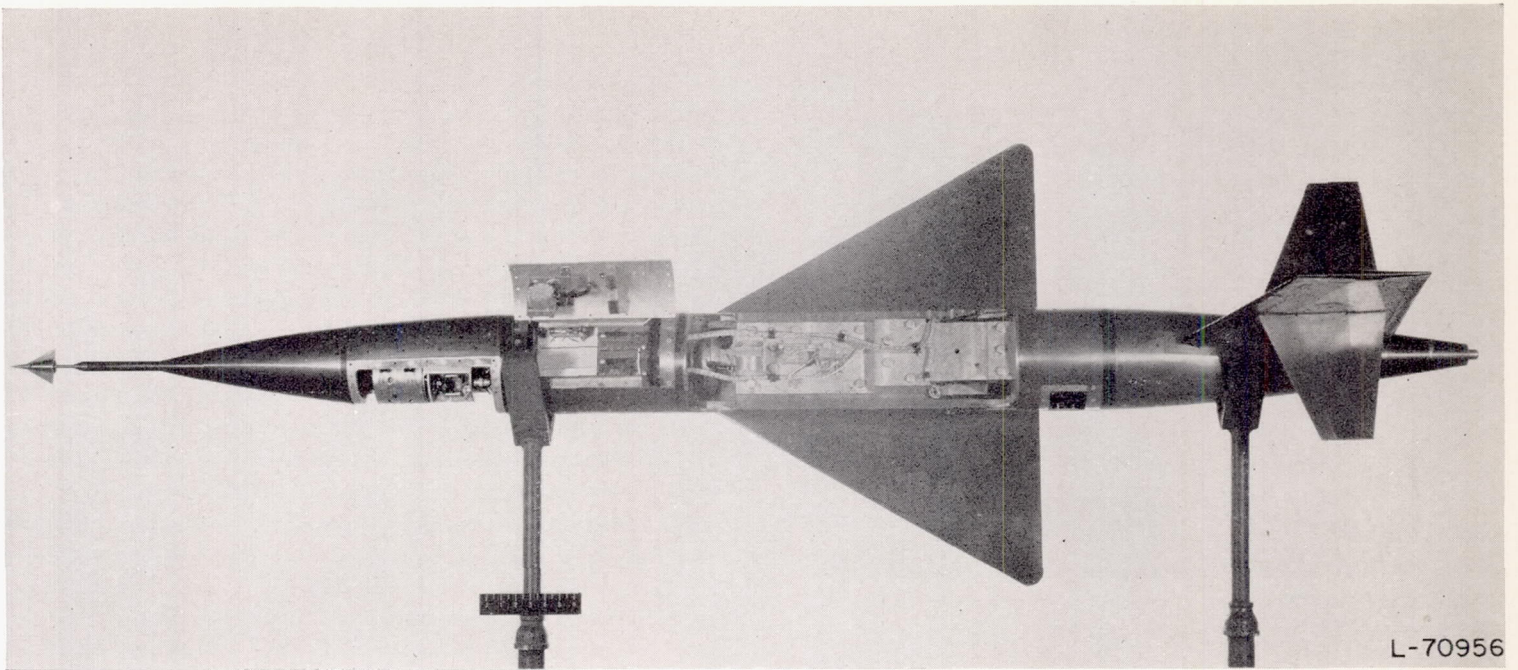
L-70956

FIGURE 5.—General view of model instrumentation.

Transverse accelerometer

Normal accelerometer

Wing balance

Total-pressure transducer

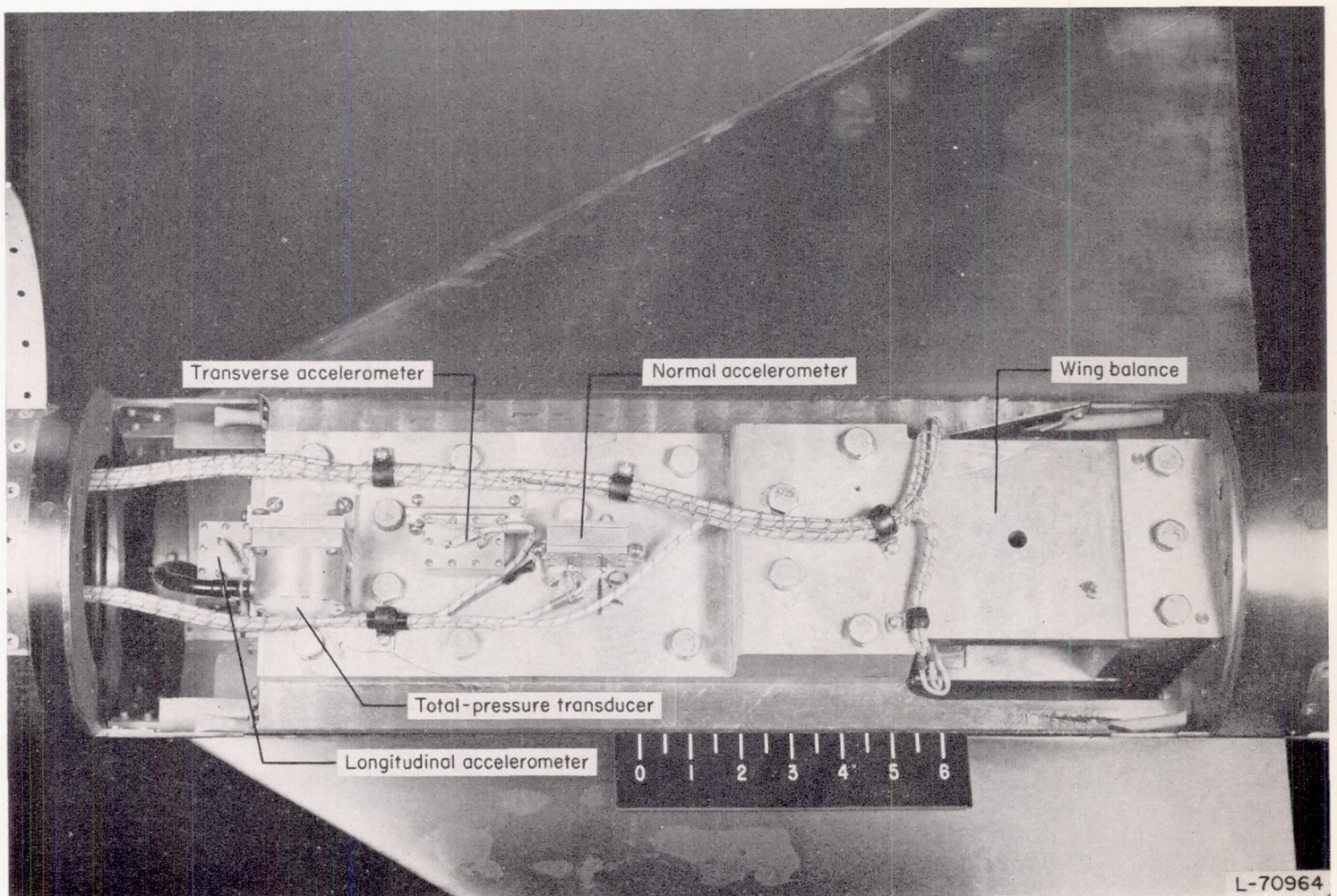Longitudinal accelerometer

0 1 2 3 4 5 6

L-70964

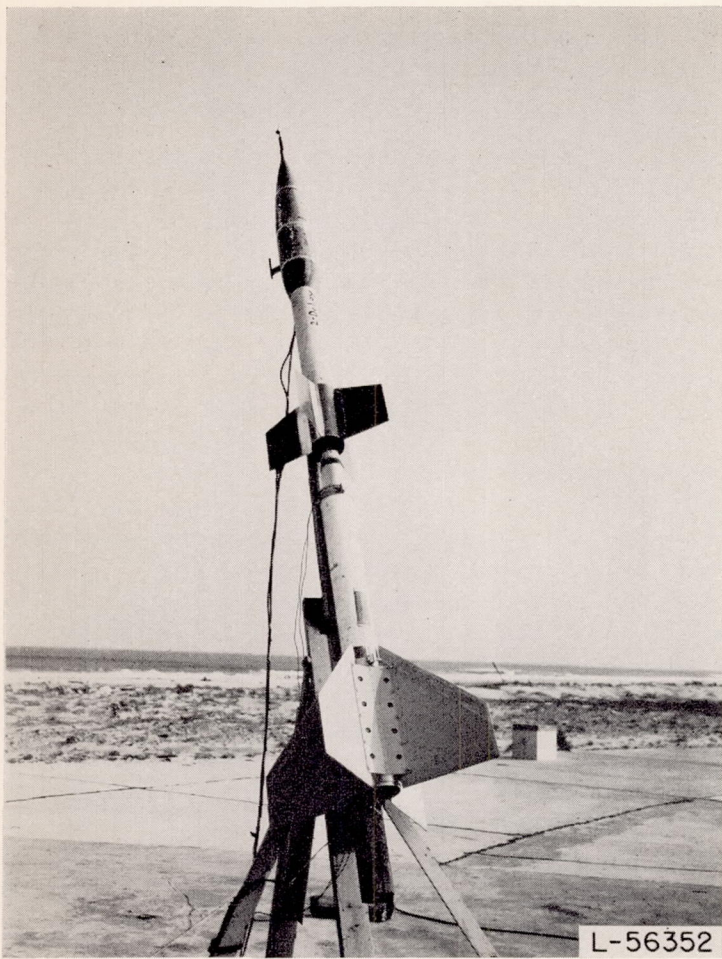FIGURE 6.—Instrumentation in center section of model.

FIGURE 7.—Test model for calibration of airspeed system.

FLIGHT TESTS

The models were launched from zero-length launchers; a typical launcher is shown in figure 11. Each model was accelerated to maximum velocity by a single 6-inch-diameter solid-propellant ABL Deacon rocket motor. The rocket was fitted with an adaptor on the forward end into which the rear end of the model fitted and with a set of cruciform fins at the rear end to provide aerodynamic stability for the model and booster combination. Small fins, with a fixed angle of incidence, were mounted on the forward ends of some of the rockets. At separation of the booster from the model these fins cause the booster to be deflected away from the flight path of the model and this deflection aided in the radar tracking of the model.

After rocket motor burnout the models separated from the boosters because of their lower drag-weight ratios compared with those of the model and booster combinations.
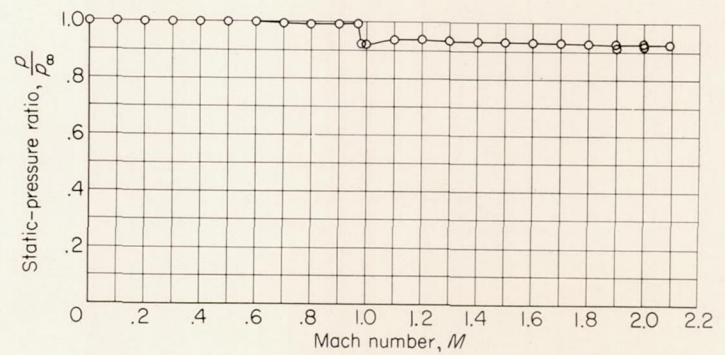

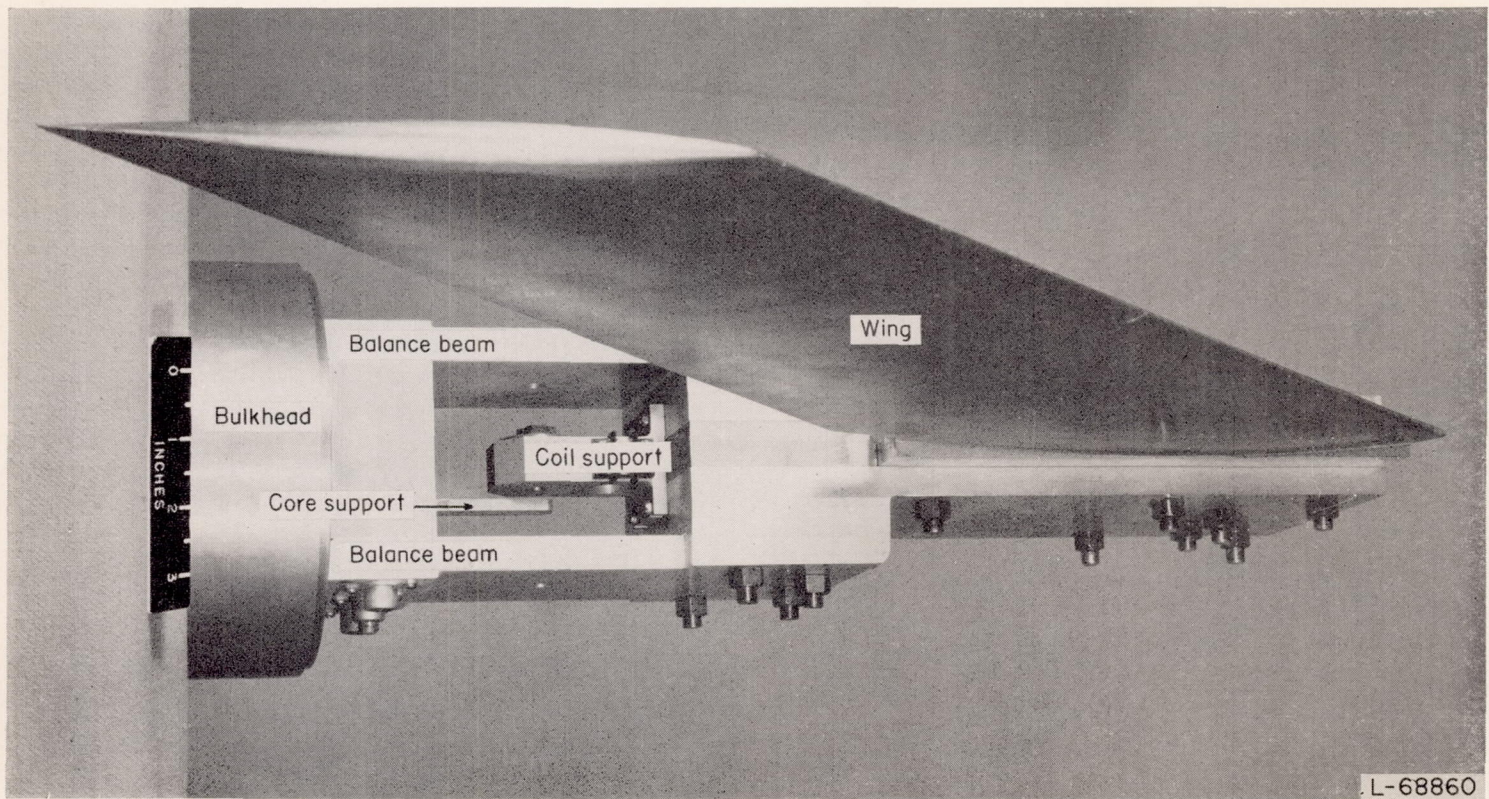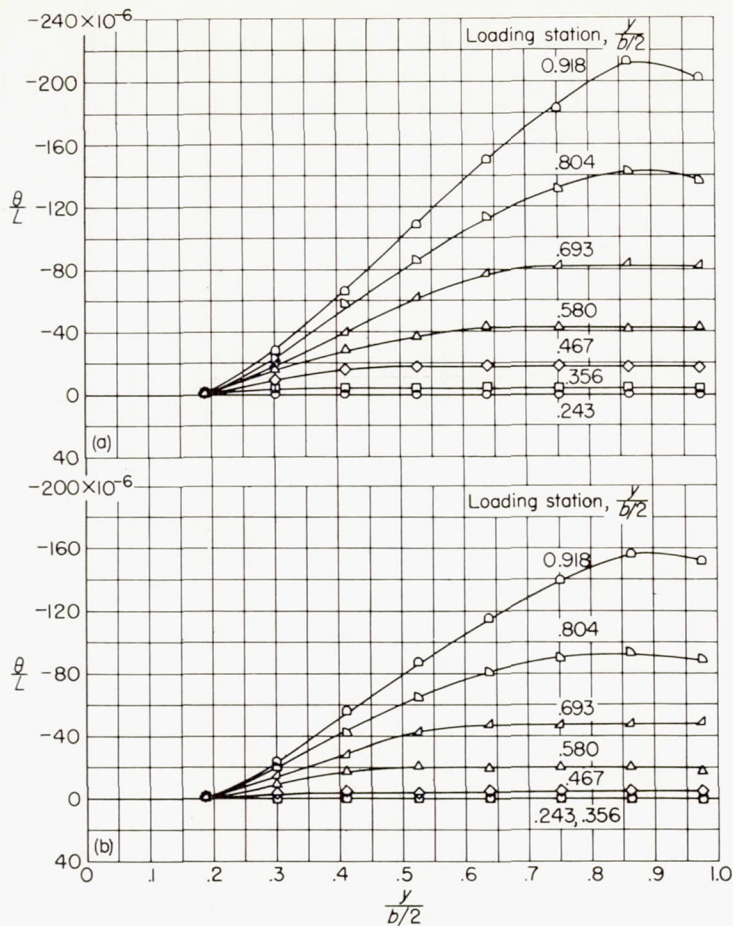FIGURE 8.—Variation of the static-pressure ratio with Mach number for the fuselage orifice.

FIGURE 9.—Wing balance components.

(a) Load applied along the 50-percent chord line.
(b) Load applied along the 25-percent chord line.

FIGURE 10.—Twist in the free-stream direction per unit load applied at various stations along the span of the duralumin wing.

TABLE III

MASS CHARACTERISTICS

| | Unswept wing | Swept | | Delta wing |
		Steel wing	Duralumin wing	
Weight, lb_____	126	146	119	142
Center of gravity, percent $\bar{c}$_____	12. 4	24. 8	4. 6	20. 6
I_Y, slug-ft²_____	8. 91	10. 30	10. 95	11. 56

The models contained no internal rocket motors and thus decelerated continuously after separation. The data used for analysis were obtained during the decelerating flight. The measurements made by the model internal instrumentation were transmitted by the telemeter to ground receiving stations. A portion of the telemeter record for the triangular-wing model, showing all quantities recorded, is given in figure 12. Disturbances in the form of abrupt stabilizer deflections between two limit positions were applied by the model control systems at predetermined time intervals during flight. The model motions during the short-period oscilla-

tions following these disturbances were analyzed to determine the aerodynamic characteristics.

DATA REDUCTION AND CORRECTIONS

The ground-based instrumentation is used to obtain a record of model velocity, Mach number, and dynamic pressure as a function of time during the model flights. The CW Doppler radar unit measures the velocity component of the model in a radial direction from the radar location. The models are launched from a point as close as possible to the radar unit so that the velocity so measured is essentially the total velocity. Model-flight-path information in the form of elevation, azimuth, and range as a function of time is obtained from the SCR 584 radar unit and is used to correct the velocity obtained by the CW Doppler radar unit to total velocity. Atmospheric conditions obtained from radiosondes are then used with the corrected velocity to obtain Mach number and dynamic pressure.

For the models discussed herein no data from the CW Doppler radar unit were obtained after separation of the models from the boosters, and for the unswept wing model no data from the SCR 584 radar unit were obtained after this point. Failure to obtain such data was due to the rapid maneuvers of the models which made tracking difficult.

When no velocity data from radar units are available, the Mach number is obtained from the standard compressible-flow equations utilizing telemetered total pressure and a static pressure obtained from radar-measured altitude and radiosonde pressures. When no radar-measured altitude information is available, the static pressure is obtained from the calibrated static orifice on the model as described previously.
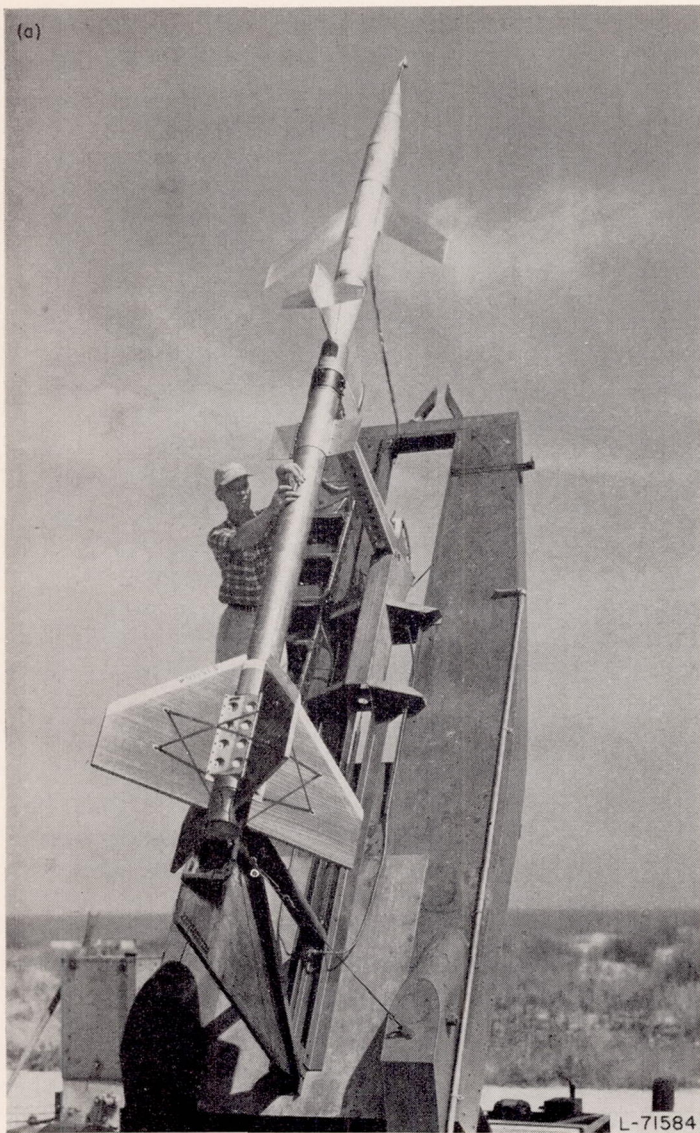
The oscillograph traces of the telemetered measurements are reduced to physical quantities by use of the calibrations of the recording equipment made immediately after each flight and the calibrations of the individual instruments made as near as possible to the time the instruments were installed in the model. The measured accelerations are then reduced to coefficient form for data-analysis purposes.

Corrections are usually required to some of the measured quantities to obtain the desired information. The accelerometers used to measure accelerations at the center of gravity can not all be located on the center of gravity, and corrections may be required to account for the distance by which the accelerometers are displaced from the desired point. These corrections must account for the effects of angular velocities and angular accelerations. For accelerometers located at distances x_a, y_a, and z_a from the center of gravity (distances positive in the direction of positive X-, Y-, and Z-axes of fig. 1), the equations for correcting accelerations to the center of gravity are:
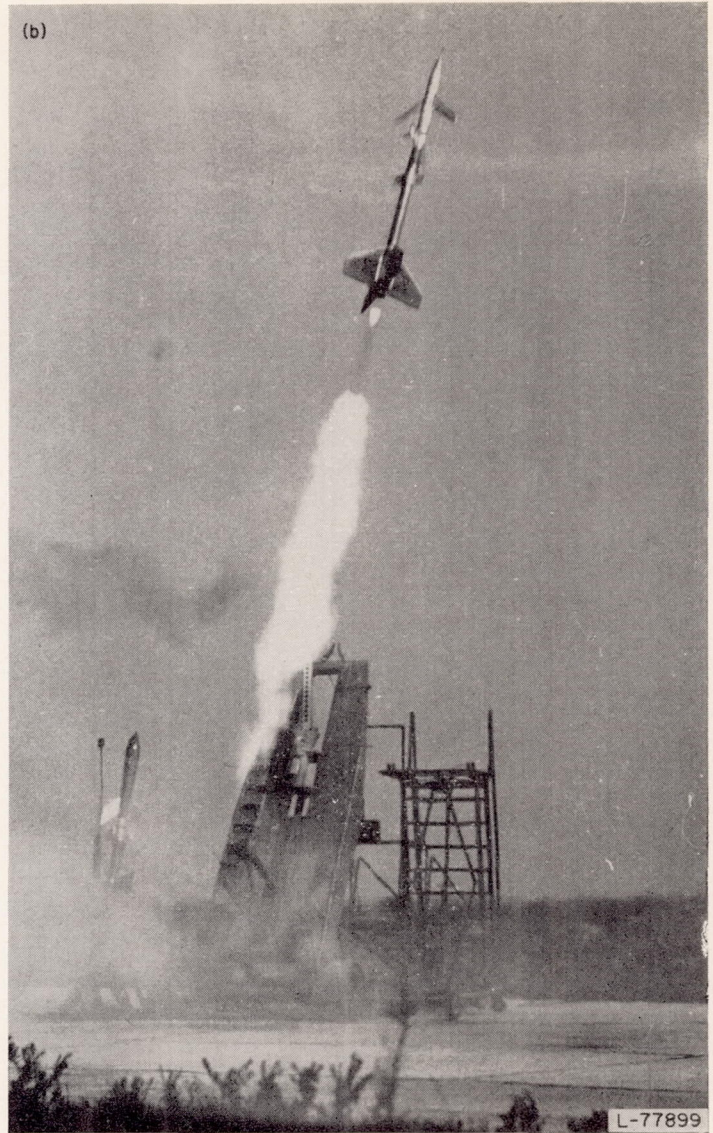
$$a_{n, cg} = a_{n, i} + \frac{1}{g} \left[-x_a(\ddot{\theta} - \dot{\psi}\dot{\varphi}) + y_a(\ddot{\varphi} + \dot{\theta}\dot{\psi}) - z_a(\dot{\varphi}^2 + \dot{\theta}^2) \right] \quad (1)$$

$$a_{t, cg} = a_{t, i} + \frac{1}{g} \left[-x_a(\ddot{\psi} + \dot{\theta}\dot{\varphi}) + y_a(\dot{\psi}^2 + \dot{\varphi}^2) + z_a(\ddot{\varphi} - \dot{\theta}\dot{\psi}) \right] \quad (2)$$

$$a_{l, cg} = a_{l, i} + \frac{1}{g} \left[x_a(\dot{\theta}^2 + \dot{\psi}^2) + y_a(\ddot{\psi} - \dot{\varphi}\dot{\theta}) - z_a(\ddot{\theta} + \dot{\psi}\dot{\varphi}) \right] \quad (3)$$

(a) Before launching.

(b) After launching.
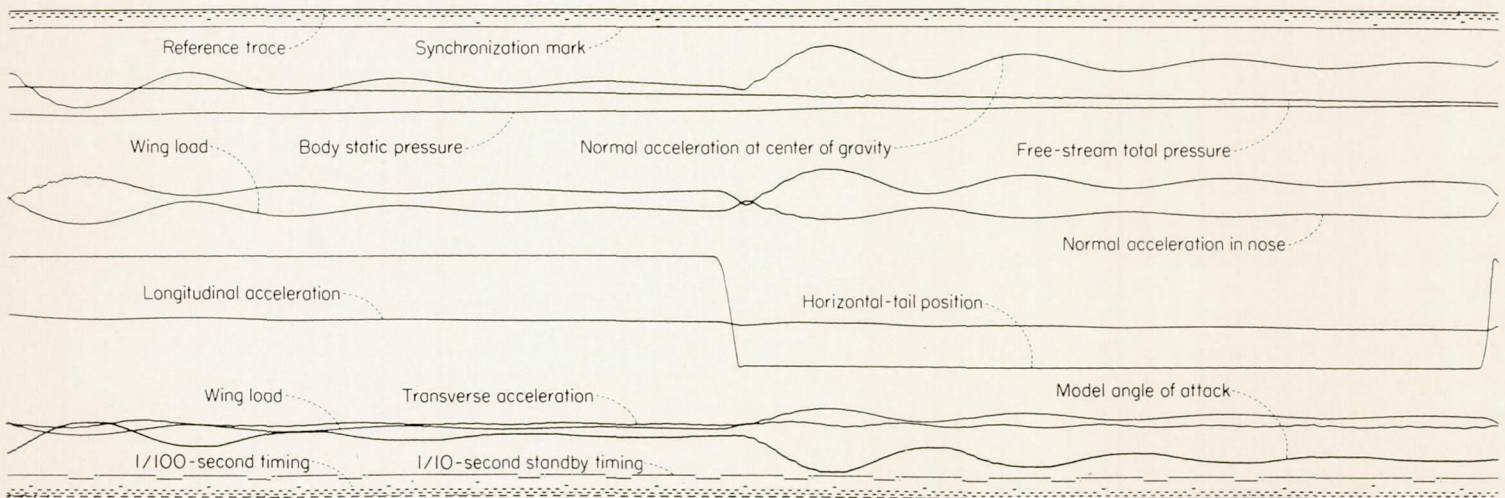
FIGURE 11.—Model launching.

FIGURE 12.—Portion of telemeter record for delta-wing model. Mach number approximately 1.1.

It is obvious that, in general, the corrections to the accelerometers are very complicated. The desirability of eliminating lateral motions is indicated since the corrections are thereby considerably simplified as follows:

$$a_{n,cg}=a_{n,i}+\frac{1}{g}\left(-z_a\dot\theta^2-x_a\ddot\theta\right) \tag{4}$$

$$a_{l,cg}=a_{l,i}+\frac{1}{g}\left(x_a\dot\theta^2-z_a\ddot\theta\right) \tag{5}$$

The pitching velocity $\dot\theta$ and angular acceleration $\ddot\theta$ may be approximated in the manner described subsequently in conjunction with analysis of the pitching-moment data.

The air-flow direction vane on the nose of the model measures angle of attack plus an increment in air-flow angularity caused by pitching velocity. The corrected angle of attack (for α and α_i in degrees) is given by

$$\alpha=\alpha_i+57.3\frac{x'}{V}\dot\theta \tag{6}$$

The wing normal forces obtained from the wing balance include not only aerodynamic forces but also inertial forces exerted by the wing and the moving parts of the balance. The total normal forces read by the balance are corrected for these inertial forces to yield the aerodynamic normal force as follows:

$$N_{aero}=N_T+a_nW_b \tag{7}$$

The resulting aerodynamic normal force is converted to coefficient form and the exposed wing lift coefficient is assumed to be given by $C_{L,w}=C_{N,w}\cos\alpha$.

Because the frequency-response characteristics of the instruments used in these tests were satisfactory, no corrections were necessary for instrument lag or amplitude attenuation effects.

METHOD OF ANALYSIS

Many mathematical procedures have been developed for analyzing transient oscillation data (refs. 7 and 8) to obtain aerodynamic derivatives. The method of analysis described herein makes use of measurements obtained during the transient oscillations resulting from step-function disturbances. The procedure adopted as a practical method of analysis was to obtain as much information as possible from direct measurements and to avoid extensive mathematical manipulation of the data. Thus problems of handling such questions as nonlinearities and the form of the derivatives could be minimized, and exploration of regions such as the stall could be conducted with little restriction. Successful application of the procedure depended upon the development of an angle-of-attack indicator with the required accuracy and frequency-response characteristics. This was successfully accomplished and is described in reference 5. Determination of some of the aerodynamic characteristics required a solution of the equations of motion, however, and this solution as well as the use of direct measurements will be described.

DIRECT MEASUREMENTS

Lift and drag.—The accelerometer measurements at the center of gravity provide normal-force and chord-force coefficients according to the following relations:

$$C_N=a_n\frac{W}{qS} \tag{8}$$

and

$$C_c=-a_l\frac{W}{qS} \tag{9}$$

The total lift and drag coefficients are then obtained from

$$C_L=C_N\cos\alpha-C_c\sin\alpha \tag{10}$$

$$C_D=C_c\cos\alpha+C_N\sin\alpha \tag{11}$$

The lift characteristics are determined by plotting lift coefficient against angle of attack. The first one or two cycles of a transient oscillation are generally used for this purpose to obtain the largest amplitudes. Such a plot may also be made during a nonoscillatory motion. The change in Mach number during one cycle of an oscillation on the flight tests reported herein was about 0.02 at supersonic speeds and about 0.007 at subsonic speeds. Thus, unless the aerodynamic parameters vary very rapidly with Mach number, the error involved in assuming that the Mach number is constant should be small. Figure 13 presents typical plots of lift coefficient as a function of angle of attack. These data are for the 45° swept-wing configuration (duralumin wing model). With the exception of the results at a Mach number of 0.92, these data were obtained for the angle of attack both increasing and decreasing with time. For this particular model the effect of rate of change of angle of attack with time is not detectable from the data. At a Mach number of 0.92, data on the variation of lift coefficient with angle of attack were obtained at angles of attack up to 18° when the model performed a pitch-up maneuver for the horizontal-tail deflection of $-4.60°$. From results such as these, the lift-curve slope (including any nonlinearities) as well as angle of zero lift, maximum lift coefficient, and the lift phenomena associated with the separated flow at high angles of attack may be determined.

The lift coefficient as determined is, of course, the total lift coefficient and includes any contributions from derivatives such as C_{L_q} and $C_{L_{\dot\alpha}}$. Normally, the effects of these contributions are negligible as indicated by the data of figure 13 but they may be calculated by using estimated values of C_{L_q} and $C_{L_{\dot\alpha}}$. Such calculations have been made for several cases and it has generally been found that, because of the phase relations between α and q, the effect of C_{L_q} and $C_{L_{\dot\alpha}}$ is to cause a slight displacement of the curves of C_L against α in such a way as to indicate a phase lead of the lift coefficient compared with the angle of attack but with no measurable change in the lift-curve slope.

The data from the wing normal-force balance are also analyzed by the direct method. Results for the swept-wing configuration are typical of the data obtained. An examination of the results (fig. 14) indicates that these data also furnish the variation of lift coefficient with both angle of attack and Mach number.
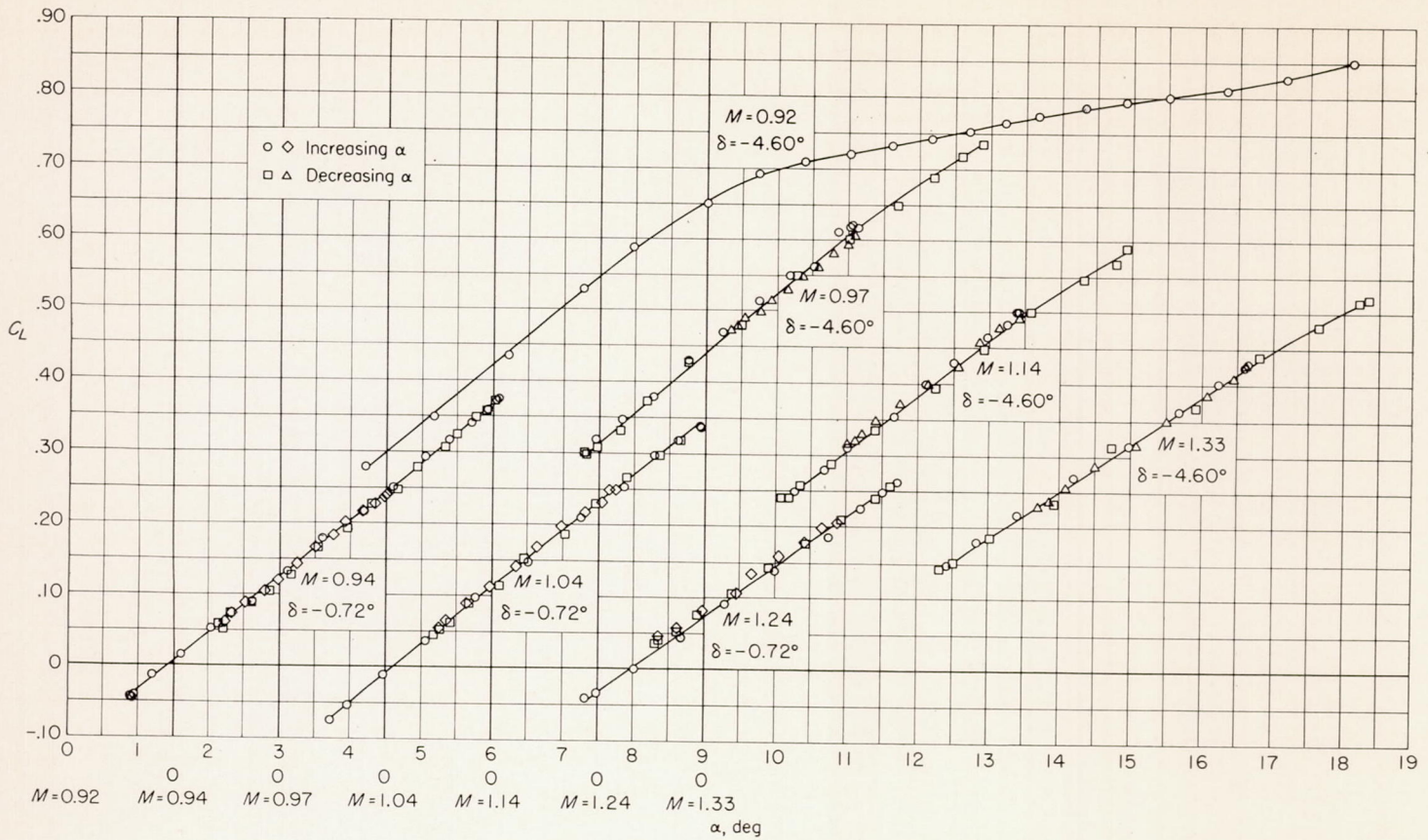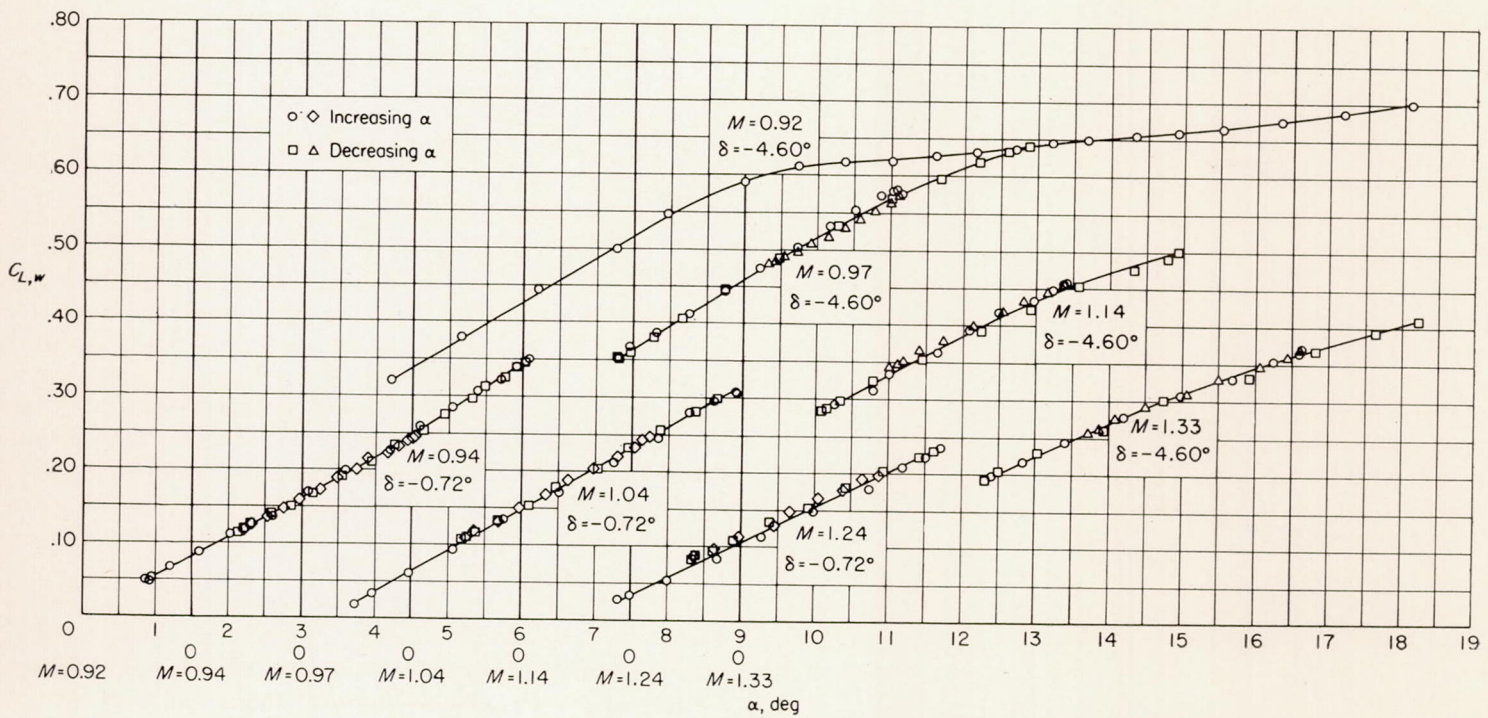
FIGURE 13.—Lift data for duralumin swept-wing model.

FIGURE 14.—Lift data for exposed wing of duralumin swept-wing model.

The drag information is generally of most use when plotted in the form of polars of C_D against C_L. Typical results are illustrated in figure 15 for the swept-wing configuration. From such plots the minimum drag coefficient and the variation of lift-drag ratio with lift coefficient may be determined. Since two control deflections are available, some measure of the increment in drag due to trimming the airplane can also be obtained. Note that only for the drag curve at a Mach number of 0.97 is the effect of the small change in Mach number significant. The oscillation represented by these data occurred during the rapid transonic drag rise.

The variation of drag with lift is sometimes represented by an equation of the form

$$C_D = C_{D,min} + K C_L^2 \qquad (12)$$

where $K = \dfrac{dC_D}{dC_L^2}$. A plot of C_D against C_L^2 will yield a linear curve whose slope is K if the preceding equation adequately represents the data. For a wing with camber or for any configuration change which produces an effective camber, the lift coefficient for minimum drag will generally not be zero, and such a drag curve may frequently be represented by the parabolic equation

$$C_D = C_{D,min} + K (C_L - C_{L,c_{D,min}})^2 \qquad (13)$$
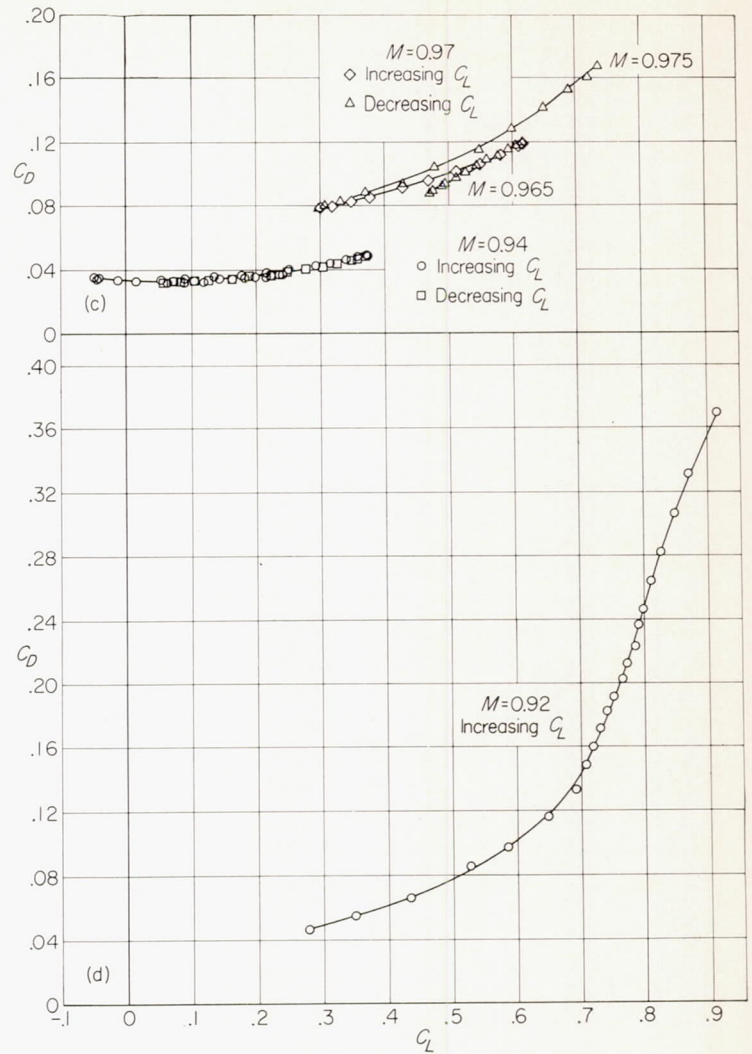
for the purpose of determining K.

Pitching moment.—The total pitching-moment coefficient is obtained from the relation

$$C_m = \frac{I_Y}{qS\bar{c}} \ddot{\theta} \qquad (14)$$
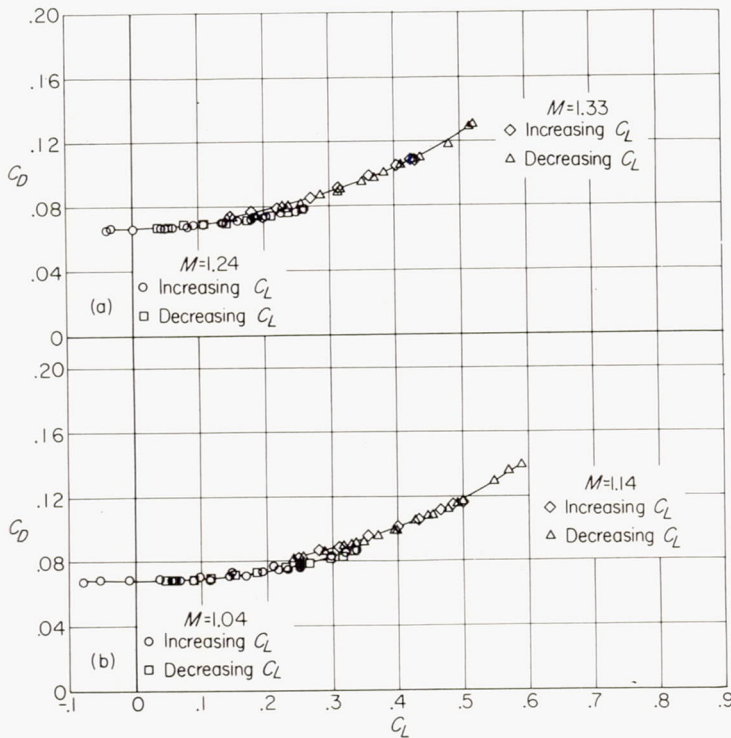
(a) Mach numbers 1.33 and 1.24.
(b) Mach numbers 1.14 and 1.04.

FIGURE 15.—Drag data for duralumin swept-wing model.

(c) Mach numbers 0.97 and 0.94.
(d) Mach number 0.92.

FIGURE 15.—Concluded.

The pitching acceleration may be measured by a pitching angular accelerometer or, as was done for some of the model results presented herein, by two normal accelerometers displaced along the longitudinal axes. With one accelerometer in the model nose and one at the center of gravity, for example, the pitching acceleration will be given by

$$\ddot{\theta} = \frac{g(a_{n,nose} - a_{n,cg})}{l} \qquad (15)$$

This result can be easily obtained from equation (4) if the z_a-distance of both accelerometers is the same. If measurements of $\ddot{\theta}$ are not available, an approximation can be found from the relations

$$\ddot{\theta} = \frac{d\dot{\theta}}{dt} \qquad (16)$$

$$\dot{\theta} = \dot{\alpha} + \dot{\gamma} \qquad (17)$$

The quantity $\dot{\alpha}$ is obtained by differentiating the measured α-curve and $\dot{\gamma}$ is calculated from the equation

$$\dot{\gamma} = \frac{g}{V}(a_{n,cg} - \cos\theta \cos\varphi) \qquad (18)$$

For the flight conditions existing on the rocket-propelled models (large q and V), the last term in the latter equation is very small and may generally be neglected; thus the need for measuring θ and φ is obviated.

The total pitching-moment coefficients obtained as described above contain contributions due to the damping terms C_{m_q} and $C_{m_{\dot{\alpha}}}$ and, unlike the corresponding lift terms, these are not usually negligible although they will generally be small compared with the pitching moments due to α. The pitching moments due to the damping terms may be subtracted from the total pitching moments to obtain pitching moments as a function of angle of attack by

$$C_m(\alpha) = C_m - \frac{\bar{c}}{2V}(C_{m_q} + C_{m_{\dot{\alpha}}})\dot{\alpha} - \frac{\bar{c}}{2V}C_{m_q}\dot{\gamma} \qquad (19)$$

where $\dot{\alpha}$ and $\dot{\gamma}$ are obtained as described previously. The sum of the damping derivatives $C_{m_q} + C_{m_{\dot{\alpha}}}$ for use in this calculation is obtained as described later. The individual value of C_{m_q} cannot be determined from the data but must be estimated for the purposes of applying this correction.

The resulting pitching-moment coefficients may be plotted against angle of attack or lift coefficient to obtain the static stability derivatives C_{m_α} and dC_m/dC_L, including nonlinear effects, the trim values of α and C_L for a given control deflection, and the value of $C_{m,0}$. From the increments in C_m for different control deflections at a constant angle of attack, a measure of the control effectiveness C_{m_δ} may be obtained. Typical pitching-moment curves are shown in

figure 16 for the swept-wing configuration. These pitching-moment data were obtained from two linear accelerometers and the results have been corrected for the previously discussed pitching moments due to the damping terms. A significant effect of Mach number during one oscillation is evident only for the curve at an average Mach number of 0.97. In this region there is apparently a rapid change in pitching moment with Mach number at a constant lift coefficient. The data at a Mach number of 0.92 are typical of results obtained when the configuration has a highly nonlinear variation of pitching-moment coefficient with lift coefficient. Note that even relatively smaller nonlinear variations, for instance at $M=0.94$, are readily apparent when the data are presented in this manner.

It is possible to analyze the data obtained from two accelerometers without first reducing the measurements to coefficient form by combining equations (14) and (15) to obtain an equation for the static stability slope dC_m/dC_L as follows:

$$\frac{dC_m}{dC_L} = -\frac{I_Y}{m\bar{c}l}\left(1 - \frac{da_{n,nose}}{da_{n,cg}}\right) \qquad (20)$$

Although the slope so determined is the rate of change of the total pitching-moment coefficient, it should be essentially unaffected by the damping moment if the slope is measured at $C_m=0$ because at this point the rate of change of the damping moment is near a minimum.

Control effectiveness.—If the amplitude of the oscillatory motions is small at the time the control-surface deflection is

(a) Horizontal-tail deflection $-4.60°$.

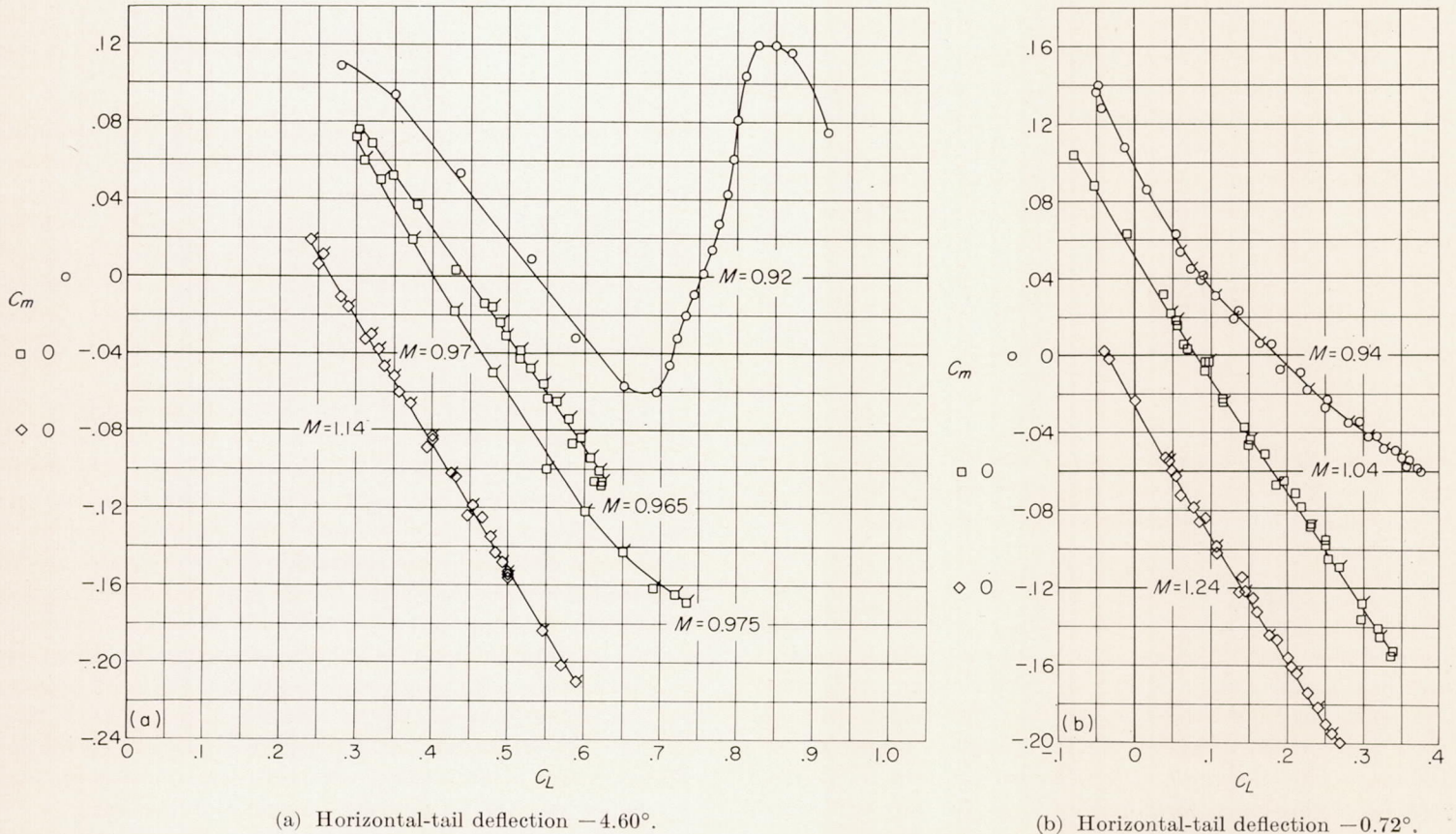(b) Horizontal-tail deflection $-0.72°$.

FIGURE 16.—Pitching-moment data for the duralumin swept-wing model as obtained from the two-accelerometer method. Flagged symbols indicate decreasing C_L.

initiated and the control movement is sufficiently rapid, the changes in lift and pitching moment due to control deflection can be detected and a direct measure of the control effectiveness parameters C_{m_δ} and C_{L_δ} can thus be obtained. For the models of the present investigation the motions were, in general, not of sufficiently small amplitude when the control motions were initiated to permit reliable values of these parameters to be determined by this method.

TRANSIENT OSCILLATION ANALYSIS

The method of analysis used herein applies to the free oscillation resulting from a disturbance. For the models considered herein, the disturbance consisted of a rapid control-surface deflection; however, other types of disturbances may be used, such as the impulse from a small rocket. The complete derivation of the equations used will not be given herein because it is fairly simple and may be found in a number of sources. Only the final results and the method of applying them to free-flight models will be shown. The discussion has been kept general in character for purposes of application to other models.

In order to simplify the analysis and to permit the determination of equations for the more important aerodynamic derivatives, several assumptions are necessary. It is assumed that, during the time interval over which each calculation is made, the following conditions hold: the forward velocity and Mach number are constant; the aerodynamic forces and moments vary linearly with α, θ, δ, $\frac{d\alpha}{dt}$, and $\frac{d\theta}{dt}$; and the model is in level flight before the disturbance is applied. A discussion of the effect of these assumptions upon the results is presented subsequently.

The first assumption mentioned in the previous paragraph effectively limits the longitudinally disturbed motion of the aircraft to two degrees of freedom: translation normal to the flight path and rotation in pitch about the center of gravity. The equations of motion resulting from these assumptions are

$$m'\left(\frac{d\theta}{dt}-\frac{d\alpha}{dt}\right)=C_{L,0}+C_{L_\alpha}\alpha+C_{L_\delta}\delta \tag{21}$$

$$I'\frac{d^2\theta}{dt^2}=C_{m,0}+C_{m_\alpha}\alpha+C_{m_{\dot\alpha}}\frac{\bar c}{2V}\frac{d\alpha}{dt}+C_{m_q}\frac{\bar c}{2V}\frac{d\theta}{dt}+C_{m_\delta}\delta \tag{22}$$

where all angular quantities are in units of radians. When these equations are solved, the following equation for the free oscillation of the angle of attack is obtained:

$$\alpha=Ce^{at}\cos(\omega t+\Omega)+\alpha_t \tag{23}$$

where C is a constant. The symbol α_t denotes the steady state or trim angle of attack which will exist after the oscillation has damped out and represents the mean value about which the angle of attack oscillates. The first term represents the oscillation about the trim angle. Figure 17 is a schematic plot showing a typical record of the angle-of-attack response following a step deflection of the aircraft control surface.

The constants a, ω, and α_t in equation (23) are independent of the initial conditions and the analysis consists essentially
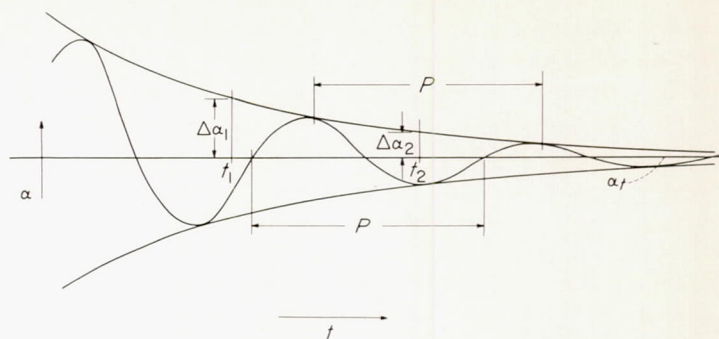

FIGURE 17.—Typical angle-of-attack oscillation as used in analysis.

of finding the numerical values of these constants from the measured data and from these constants determining the stability characteristics of the configuration tested. The constants C and Ω depend upon the initial conditions and are not used in the analysis; thus, their numerical values need not be known for the type of analysis considered herein.

From the envelope curves enclosing the oscillations, the damping constant a can be determined. If reference is made to the notation in figure 17

$$\Delta\alpha_2=\Delta\alpha_1 e^{a(t_2-t_1)} \tag{24}$$

$$a=\frac{\log_e\dfrac{\Delta\alpha_2}{\Delta\alpha_1}}{t_2-t_1} \tag{25}$$

The constant ω defines the frequency or period of the oscillation and is given by

$$\omega=\frac{2\pi}{P} \tag{26}$$

The constant α_t is simply the value of α after the oscillation has damped to a steady value or is the value of α on the mean line of the oscillation as shown in figure 17.
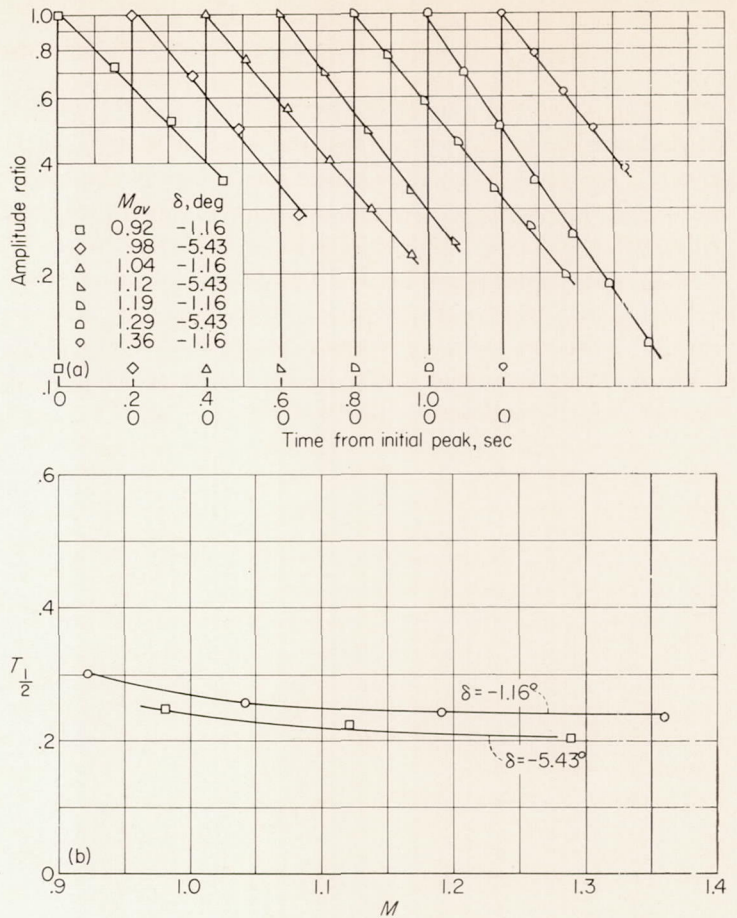
In order to determine the constants a, ω, and α_t from the measured data, it is necessary first to fair envelope curves for the oscillation which should be logarithmic curves according to equation (23). The mean line between the two envelope curves is drawn and values of $\Delta\alpha_2$, $\Delta\alpha_1$, P, and α_t can then be determined and a and ω can be calculated.

The basic data obtained from this analysis of the oscillations are usually plotted as a function of Mach number. The results of such an analysis for the delta-wing configuration are shown in figures 18 to 20. The solid lines on the trim curves in figure 18 were obtained from the mean lines of the oscillations resulting from the rapid control deflections. The period of the pitch oscillation in this case was determined by measuring the time difference for trim crossings. The data for the two different control deflections (fig. 19) define two distinct curves. Although some scatter of the data points is evident, it can be seen that a variation of period with Mach number can frequently be detected within each oscillation. The variation of amplitude ratio with time plotted on semilog paper so that straight-line fairings of the data can be utilized is illustrated in figure 20 (a). The variation with Mach number of the slope of these curves, given as time to damp to one-half amplitude, is shown in figure 20 (b). The
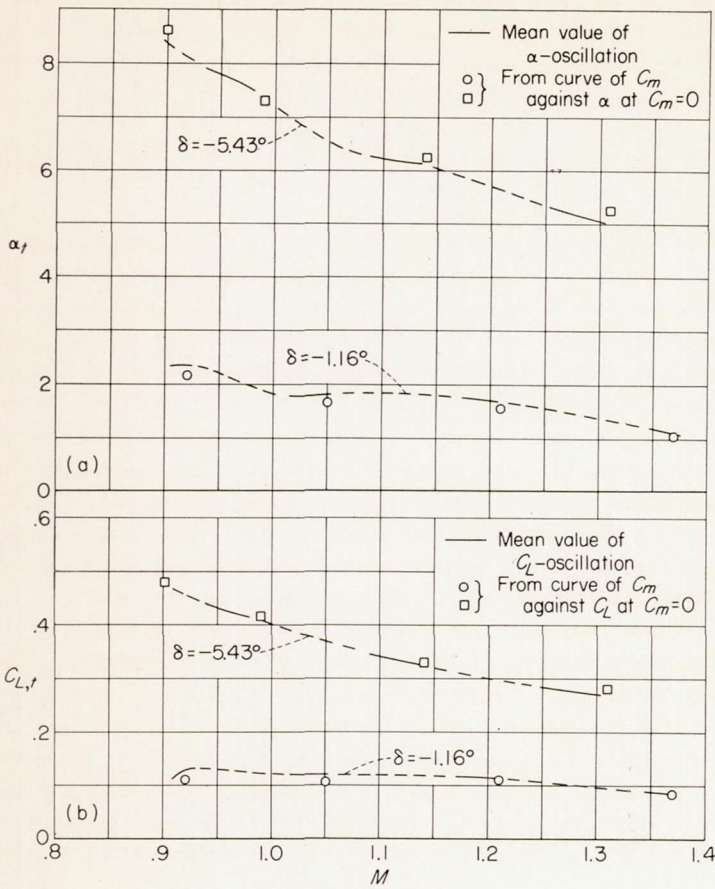
(a) Trim angle of attack.
(b) Trim lift coefficient.

FIGURE 18.—Trim lift and angle-of-attack characteristics of delta-wing model.

FIGURE 19.—Period of pitch oscillation of delta-wing model.

constant a can then be obtained from these results as

$$a = \frac{-\log_e 2}{T_{\frac{1}{2}}} = \frac{-0.693}{T_{\frac{1}{2}}} \qquad (27)$$

The success of this procedure as illustrated depends in part upon the oscillations being rather lightly damped so that several cycles are available during each oscillation to permit the fairing of envelope curves. If the oscillations are heavily damped, other methods of analysis will be necessary.

The analytical solution of equations (21) and (22), which include those aerodynamic derivatives which previous experience has indicated have an important influence on the motion, shows that the constants a and ω are given by

$$a = -\frac{1}{2}\left[\frac{C_{L_\alpha}}{m'} - (C_{m_q} + C_{m_{\dot\alpha}})\frac{\bar{c}}{2VI'} \right] \qquad (28)$$

(a) Variation of amplitude ratio with time.
(b) Time to damp to one-half amplitude.

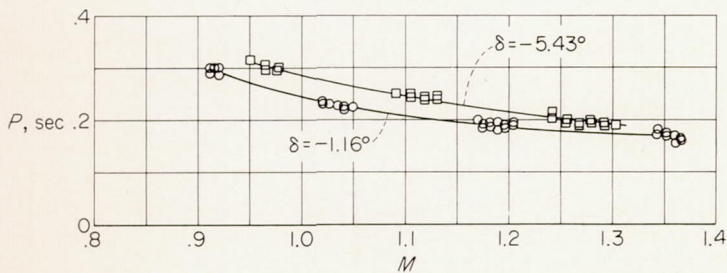FIGURE 20.—Damping-in-pitch characteristics of delta-wing model.

or

$$a = -\frac{1}{2m'}\left[C_{L_\alpha} - (C_{m_q} + C_{m_{\dot\alpha}})\frac{1}{2}\left(\frac{\bar{c}}{k_Y}\right)^2 \right] \qquad (29)$$

$$\omega = \sqrt{\frac{-C_{m_\alpha}}{I'} - \frac{\bar{c}}{2V}\left(\frac{C_{m_q} C_{L_\alpha}}{I'm'}\right) - a^2} \qquad (30)$$

The aerodynamic derivatives C_{L_q} and $C_{L_{\dot\alpha}}$ have been omitted from this analysis. The effect of these and other omitted terms upon the results is discussed subsequently. Equations (28) and (30) may be rearranged to give

$$C_{m_q} + C_{m_{\dot\alpha}} = \frac{4I'V}{\bar{c}}\left(a + \frac{C_{L_\alpha}}{2m'} \right) \qquad (31)$$

$$C_{m_\alpha} = -I'(\omega^2 + a^2) - \frac{\bar{c}}{2V}\frac{C_{m_q} C_{L_\alpha}}{m'} \qquad (32)$$

It is necessary therefore to know the value of C_{L_α} and C_{m_q} to use in equations (31) and (32) for calculating static stability and damping. The lift-curve slope C_{L_α} for use in equation (31) is found by plotting C_L against α as described previously. Numerical calculations have shown that the last term in equation (32) will probably always be very small compared with the first term (less than 1 percent) and may thus be omitted. Its effect may be estimated in any case. If this

term is omitted, the static stability parameter is then

$$C_{m_\alpha} = -I'(\omega^2 + a^2) \tag{33}$$

From C_{L_α}, a, ω, and the mass characteristics of the model, the damping factor $C_{m_q} + C_{m_{\dot\alpha}}$ and the static stability derivative C_{m_α} can be calculated by use of equations (31) and (33). The results for the delta-wing configuration shown in figures 21 and 22 are typical. Since it is obvious from figures 21 and 22 that these quantities have a nonlinear variation with angle of attack, the values obtained from the linear analysis must be considered as an average or equivalent linear value of the derivatives. The aerodynamic-center location as a fraction of the aerodynamic chord is then

$$\frac{x_{ac}}{\bar{c}} = \frac{x_{cg}}{\bar{c}} - \frac{C_{m_\alpha}}{C_{L_\alpha}} \tag{34}$$

where x_{ac} and x_{cg} are measured rearward from the leading edge of the mean aerodynamic chord.

The average longitudinal control parameters $C_{m,0}$ and C_{m_δ} can be determined from the following analysis of the trim and stability data. The equation for the steady-state angle of attack α_t obtained by solving equations (21) and (22) with $\ddot\theta$ and $\dot\alpha$ equal to zero is given by the following equation:

$$\alpha_t = \frac{-\left(C_{m,0} + \frac{C_{m_q}C_{L,0}}{m'}\frac{\bar{c}}{2V}\right) - \left(C_{m_\delta} + \frac{C_{m_q}C_{L_\delta}}{m'}\frac{\bar{c}}{2V}\right)\delta}{C_{m_\alpha} + \frac{C_{m_q}C_{L_\alpha}}{m'}\frac{\bar{c}}{2V}} \tag{35}$$

The terms in equation (35) involving $\frac{C_{m_q}}{m'}\frac{\bar{c}}{2V}$ are generally

very small and can be neglected, particularly when the airplane relative density is large. Their magnitude should, of course, be checked. When these terms are ignored, equation (35) can be expressed as

$$\alpha_t = -\frac{C_{m,0}}{C_{m_\alpha}} - \frac{C_{m_\delta}}{C_{m_\alpha}}\delta = \alpha_{t,\delta=0} + \frac{d\alpha_t}{d\delta}\delta \tag{36}$$

The values of α_t are determined for each oscillation and are then plotted against Mach number and curves faired through the data as illustrated in figure 18. The slope $d\alpha_t/d\delta$ is obtained from the increments between the curves, and $\alpha_{t,\delta=0}$ is obtained by interpolation between the two α_t-curves. From equation (36), it is now possible to calculate $C_{m,0}$ and C_{m_δ}.

An application of the above procedure to the results for the delta-wing configuration gives the values of $C_{m,0}$ and C_{m_δ} shown by the solid-line curve in figure 23. The average value of C_{m_α} from figure 21 was used with equation (35) to obtain the curves shown. The values of C_{m_δ} and $C_{m,0}$ as obtained from the previously discussed method utilizing the pitching-moment curves is shown for comparison. The agreement between the two methods of determining C_{m_δ} and $C_{m,0}$ is considered good in view of the nonlinearity of the basic pitching-moment data for this configuration.

Several procedures may now be used to determine C_{L_δ}. The value of C_{L_δ} can be obtained from the increment in C_L at any given angle of attack between the lift curves plotted for two successive oscillations at different control deflections.
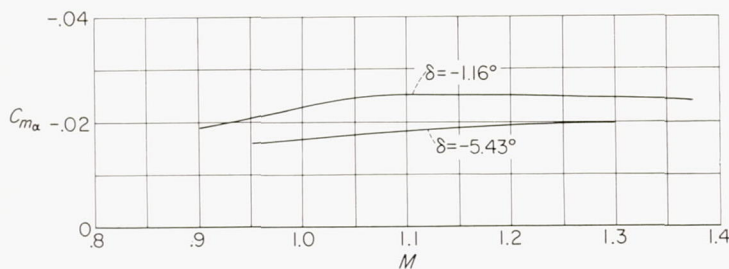

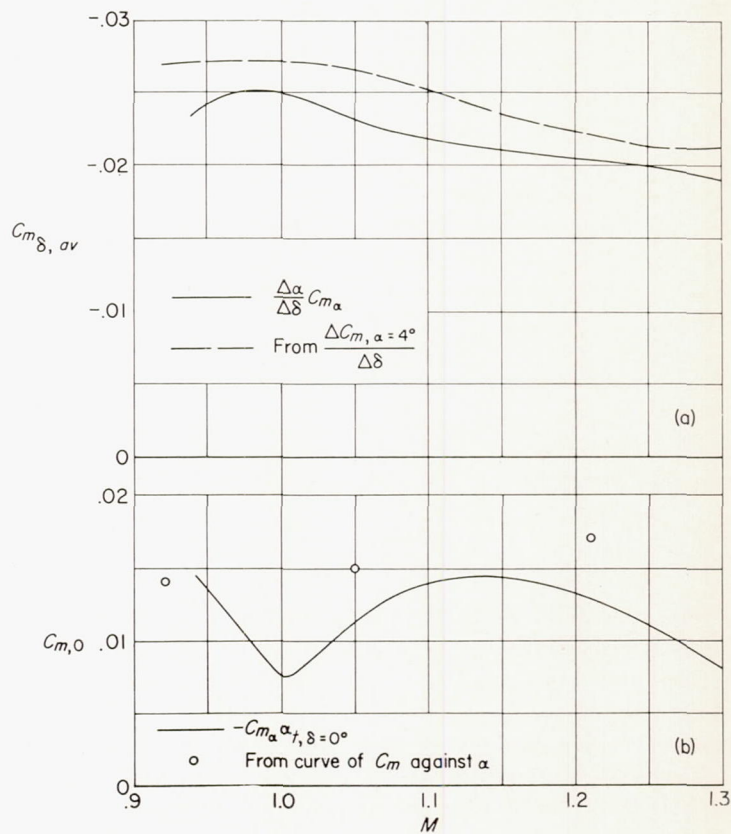FIGURE 21.—Variation of longitudinal stability parameter C_{m_α} with Mach number. Delta-wing model.
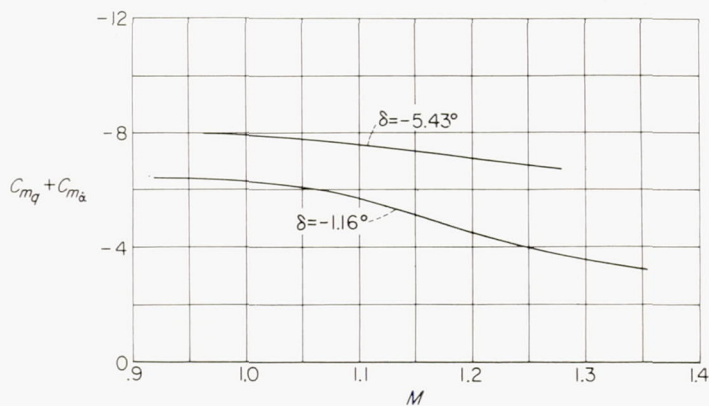
FIGURE 22.—Variation of rotary-damping coefficient with Mach number. Delta-wing model.

(a) Control effectiveness.
(b) Pitching-moment coefficient at $\alpha = \delta = 0$.

FIGURE 23.—Analysis of trim characteristics.

In equation form,

$$C_{L_\delta} = \frac{(\Delta C_L)_{\alpha=Constant}}{\Delta \delta} \qquad (37)$$

In addition, C_{L_δ} can be calculated from the equation

$$C_{L_\delta} = -C_{L_\alpha} \frac{d\alpha_t}{d\delta} + \frac{dC_{L,t}}{d\delta} \qquad (38)$$

where $dC_{L,t}/d\delta$ is found from the $C_{L,t}$ and δ curves in the same manner as $d\alpha_t/d\delta$. Another check on the value of C_{L_δ} can be obtained from

$$C_{L_\delta} = -\frac{C_{m_\delta}}{l_t/\bar{c}} \qquad (39)$$

where $l_t/\bar{c}$ is the longitudinal distance from the center of gravity to the center of pressure of the lift caused by control-surface deflection. For a conventional airplane configuration with a horizontal tail, this distance can be estimated fairly accurately.

The three methods given for determining C_{L_δ} are not all equally applicable to all configurations. For an airplane with a conventional tail surface to the rear of the wing, the value of C_{L_δ} is usually small, and the distance to the center of pressure of the lift due to control deflection can be estimated fairly accurately. Equation (39) should then give the most reliable results for C_{L_δ}. Conversely, for a configuration having all-movable wings near the center of gravity C_{L_δ} is of the same order of magnitude as C_{L_α} and the distance to the center of pressure of the lift due to control deflection cannot be accurately estimated, since this lift includes an increment caused by wing downwash on the tail. For this case equations (37) and (38) should give a more reliable result.

Figure 24 presents a comparison of the results obtained on the unswept-wing configuration by using the three methods. For this particular configuration it is not readily apparent from the data which method gives the most consistent results
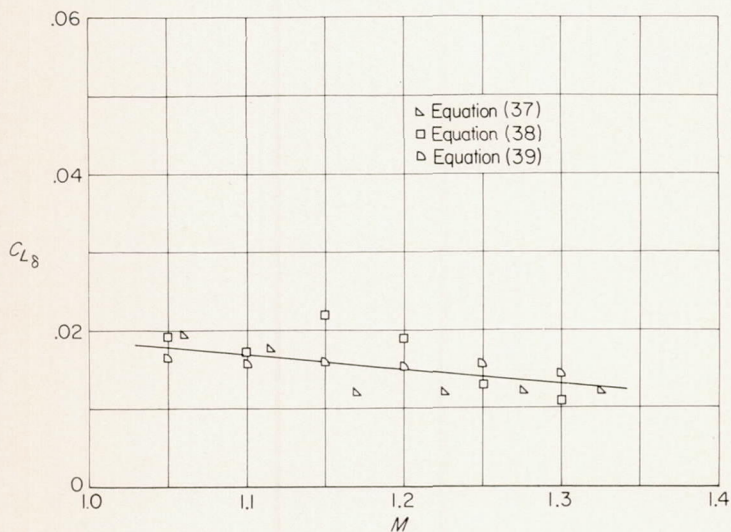

FIGURE 24.—Comparison of three methods of determining tail lift effectiveness. Unswept-wing model.

but from the previous discussion the results from equation (39) are considered to be the most reliable.

EFFECT OF ASSUMPTIONS IN ANALYSIS

The method of analysis described and illustrated herein has been developed by use of a number of simplifying assumptions, as noted in the analysis section. It is instructive to examine some of these assumptions to determine their validity where possible.

One of the assumptions was that of constant forward velocity. The variable forward velocity which actually existed during the model flights may be considered to have several effects: (1) the small perturbation velocity which is present when the third degree of freedom of the longitudinal motion is permitted; (2) the variation in the mean velocity, consisting of an essentially constant deceleration over a small time interval; (3) the effect of unsteady air flow on the aerodynamic characteristics of the various components of the aircraft; and (4) the variation of the aerodynamic derivatives with Mach number.

The effects of the small perturbation velocities may be considered by comparing the calculated motions from a two-degree-of-freedom system of equations with those from a three-degree-of-freedom system. This comparison was made by using the characteristics of the unswept wing model of this report. Adding the third degree of freedom caused a change in oscillation period and damping of less than 1 percent which is small compared with the overall test and data-reduction accuracies.

The effects of a variation in the mean velocity have been considered by several investigators (refs. 9 and 10), and it has been found that a first-order effect of acceleration consists of the addition of terms dependent on $\dot{V}/V^2$ to the damping and frequency constants of the motion. A numerical check, using the experimental data from this report, indicates that the deceleration existing during the time the experimental data were obtained could cause a change in damping of less than 1 percent and a very much smaller change in period.

Reference 11 investigates analytically the effect of accelerated air flow on the pressure drag and lift-curve slope of thin wings in the transonic and supersonic speed ranges. The wing is considered as decelerating from supersonic speeds, and this condition actually exists for the rocket-propelled models. The largest effect occurs at a Mach number of 1.0 where for unaccelerated air flow the aerodynamic quantities are infinite and for decelerating air flow the aerodynamic quantities are finite. Numerical calculations in reference 11 indicate that, at $M=1.02$, for example, the pressure drag of a wedge airfoil and the lift-curve slope of a flat-plate airfoil of the size on the models discussed in this report would be decreased by 16 percent if the airfoil were decelerating at a rate of $376g$. The actual deceleration obtained on the models herein was about $4g$ at supersonic speeds. This effect may therefore be considered negligible.

Since the model is decelerating, the Mach number will change during each oscillation and the aerodynamic derivatives will also change. The values obtained in the analysis are thus average values over a small Mach number interval.

The effect of the varying Mach number on the calculated results is minimized by determining the required information over the shortest possible time interval. The lift-curve slope can be determined during one-half cycle of an oscillation, for instance. The static-stability derivative C_{m_α} can be obtained by measuring each half-period and multiplying by two, plotting the results against Mach number, and making the computations from a faired curve as shown in figure 19. The damping time can also be measured several times during an oscillation and plotted against Mach number. Similarly, the values of $C_{L,0}$, $C_{L,t}$, and α_t can be determined for each oscillation and plotted against Mach number; the quantities α_{L0}, $dC_{L,t}/d\delta$, $d\alpha_t/d\delta$, and $\alpha_{t,\delta=0}$ can be obtained from faired curves through the points rather than from the increments between measured points at different Mach numbers. The change in Mach number during the flight tests for one cycle of an oscillation was about 0.02 at supersonic speeds and about 0.007 at subsonic speeds. Thus, unless the aerodynamic parameters vary very rapidly with Mach number, the error involved in assuming that the Mach number is constant should be small.

The method of analysis is not strictly valid if the aerodynamic derivatives are not constant at a given Mach number. The primary effects of such nonlinearities can be determined, however, by choosing control-surface deflections which cause the model to oscillate over different ranges of angle of attack. This effect was evident on two of the model flights described in this report where different values of C_{L_α} and C_{m_α} were obtained for positive and negative control deflections in the transonic region. If the aerodynamic derivatives are extremely nonlinear within the region covered by one oscillation, then the values obtained in the analysis are only average values indicative of the trend of the data.

Certain of the derivatives can be nonlinear without seriously affecting the results. For example, the period of the oscillation is almost completely determined by C_{m_α}, all other terms having only a very small influence; thus, nonlinearities in all other derivatives would not appreciably affect the calculated values of C_{m_α}. Considerable judgment is necessary in interpreting the data when evidences of nonlinearities exist and other more laborious methods of analysis may be necessary.

When the three-degree-of-freedom calculations were made, certain other effects were also investigated. These were the effects on period and damping of the omission of C_{L_q} and $C_{L_{\dot\alpha}}$ from the analysis and the effects of the assumption of zero mean flight-path angle. For the flight conditions of the models discussed herein, these effects were negligible.
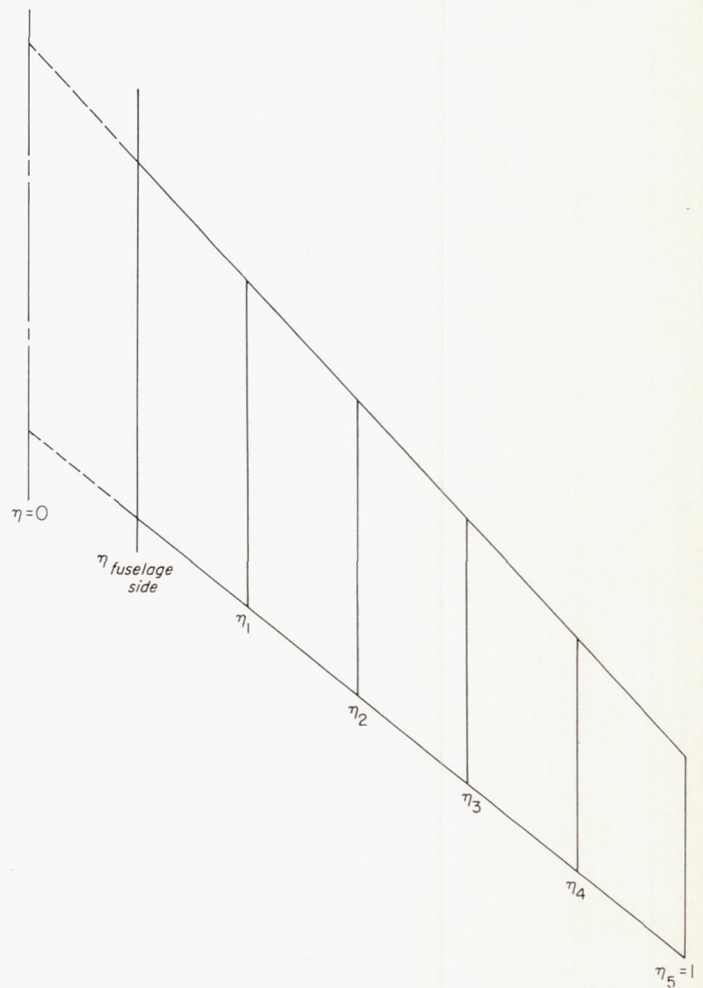
AEROELASTIC ANALYSIS

The method used to estimate the change in lift and center of pressure due to elastic deflection of the swept wings is a form of strip theory. The information needed to apply this method is data on twist along the wing due to unit loads applied along the centers of pressure (assumed to be along the 0.25 and 0.50 chord line), an assumed rigid-wing span-loading curve, and an estimate of the rigid-wing lift-curve slope.
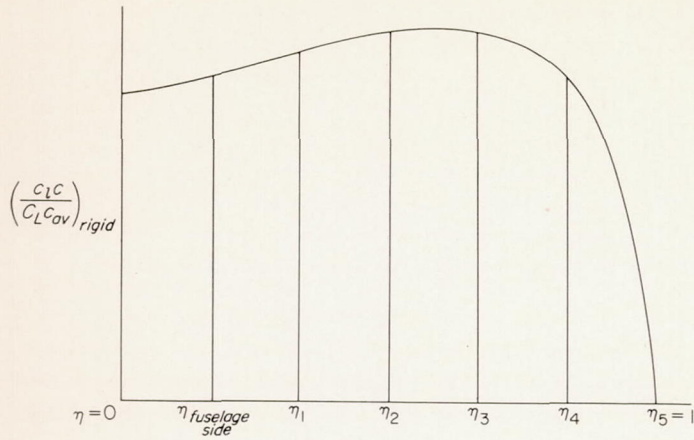
The portion of the half wing which is elastic (that portion outside of the fuselage) is divided into as many parts as desired. The rigid lift per unit angle of attack of these sections is then estimated from the span loading. The increment in lift due to twist at the section is then assumed to be given by this lift-curve slope multiplied by the twist. Since the twist at a given section depends on the final equilibrium lift at all sections, a set of n simultaneous equations (equal in number to the number of sections the wing is divided into) must be solved; this solution gives the resultant elastic lift at each section. The equations are set up by use of the ratio of the elastic lift at each section to the rigid lift at the section. The independent variable used in the equations is the rigid lift-curve slope times the dynamic pressure $C_{L_{\alpha,r}}q$.

Drawings for the exposed-wing panel and span-loading curve divided into five sections are given in sketches 1 and 2. The equations for each section of the exposed-wing panel are

$$
\left.
\begin{aligned}
L_1 &= K'Q\,\frac{S}{2}\int_{\substack{\eta_{fuselage}\\side}}^{\eta_1}\left(\frac{c_l c}{C_L c_{av}}\right)_{rigid} d\eta(\alpha_r+\Delta\alpha_1)\\
\cdot\qquad\cdot\qquad\cdot\qquad\cdot\qquad\cdot\\
L_5 &= K'Q\,\frac{S}{2}\int_{\eta_4}^{1}\left(\frac{c_l c}{C_L c_{av}}\right)_{rigid} d\eta(\alpha_r+\Delta\alpha_5)
\end{aligned}
\right\}
\tag{40}
$$

$\eta=0$

$\eta_{fuselage\,side}$

η_1

η_2

η_3

η_4

$\eta_5=1$

Sketch 1.

Sketch 2.

where the L-terms are the loads on each section of the exposed wing, $\eta=\dfrac{y}{b/2}$, $K'=\dfrac{1}{\displaystyle\int_{\eta_{fuselage\atop side}}^{1}\left(\dfrac{c_l c}{C_L c_{av}}\right)_{rigid} d\eta}$, Q is defined

as $C_{L_{\alpha,T,w}}q$, and $K_1, K_2, \ldots K_5$ are defined as follows:

$$K_1=K'\,\frac{S}{2}\int_{\eta}^{\eta_1}\left(\frac{c_l c}{C_L c_{av}}\right)_{rigid} d\eta \\ \cdot \qquad \cdot \qquad \cdot \qquad \cdot \qquad \cdot \\ K_5=K'\,\frac{S}{2}\int_{\eta_4}^{1}\left(\frac{c_l c}{C_L c_{av}}\right)_{rigid} d\eta \Bigg\} \quad (41)$$

The ratio of the twist at each section to the rigid angle of attack can be derived from equations (40) and (41) for the following expressions:

$$\frac{\Delta\alpha_1}{\alpha_r}=\frac{L_1}{\alpha_r K_1 Q}-1 \\ \cdot \quad \cdot \quad \cdot \quad \cdot \quad \cdot \\ \frac{\Delta\alpha_5}{\alpha_r}=\frac{L_5}{\alpha_r K_5 Q}-1 \Bigg\} \quad (42)$$

The influence coefficient θ_{ij} is defined as the twist at station i due to a unit load applied at station j, and the equations for the twist of each wing section due to loads $L_1, L_2, \ldots L_5$ are as follows:

$$\frac{\Delta\alpha_1}{\alpha_r}=\frac{L_1}{\alpha_r}\theta_{11}+\frac{L_2}{\alpha_r}\theta_{12}+\frac{L_3}{\alpha_r}\theta_{13}+\frac{L_4}{\alpha_r}\theta_{14}+\frac{L_5}{\alpha_r}\theta_{15} \\ \cdot \qquad \cdot \qquad \cdot \qquad \cdot \qquad \cdot \\ \frac{\Delta\alpha_5}{\alpha_r}=\frac{L_1}{\alpha_r}\theta_{51}+\frac{L_2}{\alpha_r}\theta_{52}+\frac{L_3}{\alpha_r}\theta_{53}+\frac{L_4}{\alpha_r}\theta_{54}+\frac{L_5}{\alpha_r}\theta_{55} \Bigg\} \quad (43)$$

When equations (42) are substituted into equations (43) for $\Delta\alpha_1/\alpha_r$, $\Delta\alpha_2/\alpha_r \ldots \Delta\alpha_5/\alpha_r$, the following set of five simultaneous equations is obtained with Q as the independent variable:

$$\frac{L_1}{\alpha_r}\left(\theta_{11}-\frac{1}{K_1 Q}\right)+\frac{L_2}{\alpha_r}\theta_{12}+\frac{L_3}{\alpha_r}\theta_{13}+\frac{L_4}{\alpha_r}\theta_{14}+\frac{L_5}{\alpha_r}\theta_{15}=-1 \\ \cdot \qquad \cdot \qquad \cdot \qquad \cdot \qquad \cdot \\ \frac{L_1}{\alpha_r}\theta_{51}+\frac{L_2}{\alpha_r}\theta_{52}+\frac{L_3}{\alpha_r}\theta_{53}+\frac{L_4}{\alpha_r}\theta_{54}+\frac{L_5}{\alpha_r}\left(\theta_{55}-\frac{1}{K_5 Q}\right)=-1 \Bigg\} \quad (44)$$

After equations (44) are solved for L_1/α_r, $L_2/\alpha_r \ldots L_5/\alpha_r$ for each value of Q,

$$\left(\frac{C_{L_{\alpha,e}}}{C_{L_{\alpha,T}}}\right)_w=\frac{2\left(\dfrac{L_1}{\alpha_r}+\dfrac{L_2}{\alpha_r}+\dfrac{L_3}{\alpha_r}+\dfrac{L_4}{\alpha_r}+\dfrac{L_5}{\alpha_r}\right)}{QS} \quad (45)$$

for the exposed wing.

The effect of wing-inertia loading acting in opposition to aerodynamic loading has been neglected in equations (44). The addition of a wing-inertia term for a case where the wing is divided into two sections is illustrated in sketch 3:
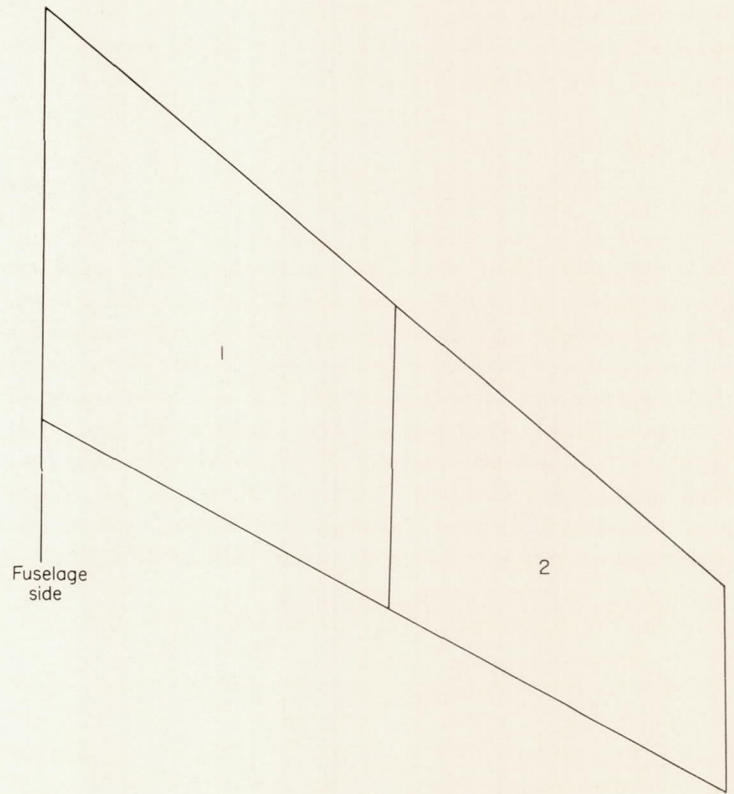
Sketch 3.

$$\frac{\Delta\alpha_1}{\alpha_r}=\frac{L_1}{\alpha_r}\theta_{11}+\frac{L_2}{\alpha_r}\theta_{12}-\frac{1}{W}\frac{L_T}{\alpha_r}(W_1\theta_{11}+W_2\theta_{12})=\frac{1}{K_1 Q}\frac{L_1}{\alpha_r}-1 \\ \frac{\Delta\alpha_2}{\alpha_r}=\frac{L_1}{\alpha_r}\theta_{21}+\frac{L_2}{\alpha_r}\theta_{22}-\frac{1}{W}\frac{L_T}{\alpha_r}(W_1\theta_{21}+W_2\theta_{22})=\frac{1}{K_2 Q}\frac{L_2}{\alpha_r}-1 \Bigg\} \quad (46)$$

where
W total model weight
W_1 weight of inboard section of exposed half-wing
W_2 weight of outboard section of exposed half-wing
L_T total lift of model

The inboard movement in the spanwise center of pressure which results from the reduction in lift due to aeroelastic wing twist causes a change in aerodynamic-center position. The lateral center of pressure of the exposed elastic wing can be found from L_1/α_r, L_2/α_r, . . . L_5/α_r solved from the simultaneous equations (44) as follows:

$$(y'_{cp})_e = \frac{L_1 y'_1 + L_2 y'_2 + L_3 y'_3 + L_4 y'_4 + L_5 y'_5}{L_1 + L_2 + L_3 + L_4 + L_5} \quad (47)$$

If the span load is assumed to move inboard along the half- or quarter-chord line, the increment in aerodynamic-center position of the complete model due to the inboard movement can be found from the following expression:

$$\Delta \frac{\partial C_m}{\partial C_L} = \left[\frac{(y'_{cp})_r - (y'_{cp})_e}{\overline{c}} \tan \Lambda \right] \frac{C_{L_{\alpha,w}}}{C_{L_{\alpha,T}}} \quad (48)$$

For the tan Λ use either tan $\Lambda_{c/4}$ or tan $\Lambda_{c/2}$ whichever is appropriate.

An application of this aeroelastic analysis to the swept-wing configuration illustrates the usefulness of the results. If the aeroelastic effect is represented by a one-point solution, the following result will be obtained:

$$\frac{1}{C_{L_{\alpha,e}}} \propto qS \left(\frac{\theta}{L} \right)_{ref} \quad (49)$$

This simplified result is useful in determining rigid values of lift-curve slope from measured elastic values. An application of this result is given in figure 25. The results shown are for the steel and duralumin swept-wing models and an additional point from some results (ref. 12) for a configuration having the same wing but constructed of wood and duralumin. Two different values of $(\theta/L)_{ref}$ were used, one for a load applied on the 0.50 chord and the other for a load applied on the 0.25 chord. Straight lines through either set of points have a common point of intersection at $qS(\theta/L)_{ref} = 0$. This may be taken as the rigid value of $\frac{1}{C_{L_\alpha}}$.
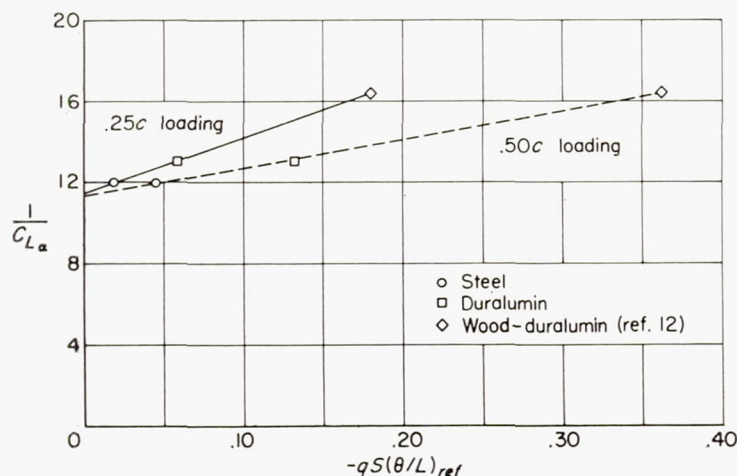
Measurements of the lift-curve slope of the steel and duralumin swept-wing models were extrapolated to rigid values of lift-curve slope by the method indicated previously. These values of rigid wing lift-curve slope and the measured influence coefficients of figure 10 were used with equations (44) to calculate the ratio of the elastic lift-curve slope to the rigid lift-curve slope. The agreement between the calculated and measured results shown in figure 26 indicates the validity of the aeroelastic analysis method described.

ACCURACY

The accuracy of the results from any one test cannot be precisely defined. The following discussion of the probable order of magnitude of the accuracy was obtained from a consideration of the accumulated experience from repeated calibrations of the instruments and recording equipment and of flight test experience where duplicate models were flown or duplicate measurements made by different instrumentation.

The absolute magnitude of a telemetered quantity will in most cases be accurate to within 1 percent of the total calibrated range and the errors will very seldom exceed 2 percent. The incremental values or rates of change of the telemetered quantities should be accurate to 1 percent or better in almost all cases. For maneuvering models, such as those described herein, the radar equipment will generally give results accurate to about 1 percent in the early portions of flight with errors greater than 1 percent in later portions.

Based on the foregoing and other considerations, the estimated probable accuracy of some of the basic quantities involved in the tests is given in table IV. The accuracy of a_l for the unswept-wing model is considerably less than that for the other models because the accelerometer was calibrated to cover a much greater range of acceleration in order to include the accelerating portion of flight during boost as well as the decelerating portion, whereas for the

FIGURE 25.—Variation of reciprocal of model lift-curve slope with wing stiffness at $M=1.11$.
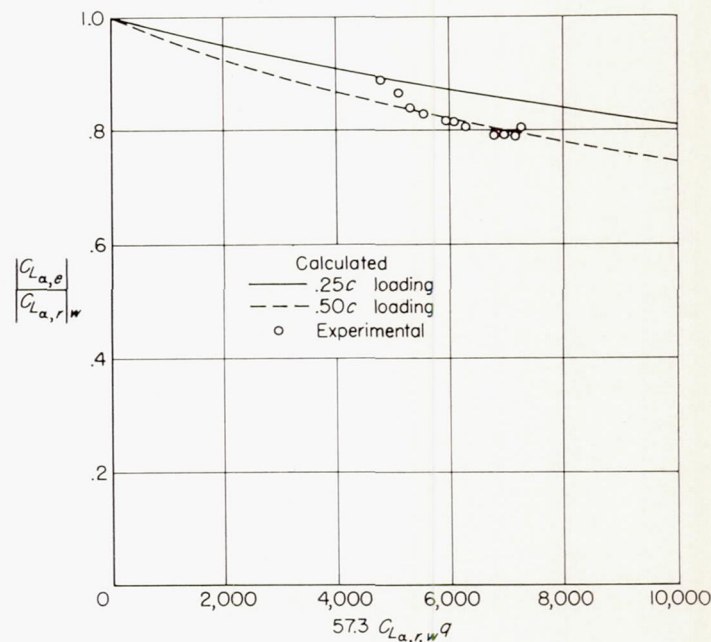

FIGURE 26.—Comparison between experimental and calculated elastic to rigid lift-curve-slope ratios for the duralumin swept wing.

other models the longitudinal accelerometers were calibrated to include the decelerating portion plus $1g$ positive acceleration and were thus against stops during boost. The effects of the estimated accuracies of these basic quantities on some of the derived aerodynamic parameters are given in table V. In these tables certain quantities are included as ratios, such as $\frac{da_n}{d\alpha}$ and $\frac{da_{n,\,nose}}{da_{n,\,cg}}$, because these ratios determine the accuracy of C_{L_α} and $\frac{x_{ac}}{\bar{c}}$, respectively, rather than the absolute values of each quantity. The calculated accuracies of $C_{m_q}+C_{m_{\dot\alpha}}$ are given in percent rather than as absolute magnitudes because the values of $C_{m_q}+C_{m_{\dot\alpha}}$ have widely different numerical magnitudes for the three configurations flown in this investigation.

Based on reference 13, the estimated possible error of each parameter is then the root-mean-square value of all the additive errors listed in table V, and these root-mean-square values are also given in table V.

DISCUSSION

SUMMARY OF RESULTS

Lift.—The variations with Mach number of the total lift-curve slopes and the exposed-wing lift-curve slopes are shown in figure 27 for the four models as obtained from plots of C_L against α as in figures 13 and 14. Data were obtained to lower Mach numbers for the unswept-wing model than for the other three models because this model did not pitch up at high angles of attack and execute violent lateral and longitudinal motions as did the other three models.

The data for the delta-wing model (fig. 27 (a)) indicated nonlinearity with lift coefficient over the entire Mach number range with the lift-curve slope of the total configuration at the high lifts being somewhat lower than that at the lower lifts. It is believed that this condition primarily resulted from the horizontal tail being in a position such that the downwash variation with angle of attack $d\epsilon/d\alpha$

TABLE IV

ESTIMATED ACCURACIES OF BASIC QUANTITIES

[All increments may be positive or negative]

Quantity	Estimated accuracy for—	
	$M=1.35$	$M=0.9$
M	0.015	0.030
W, lb	1.0	1.0
Center-of-gravity position, in.	0.06	0.06
q, percent	2.5	6.0
I_Y, percent	2.0	2.0
a_n, g units	0.5	0.5
a_l:		
Unswept-wing model, g units	0.4	0.4
All other models, g units	0.1	0.1
α, deg	0.5	0.5
$\frac{da_{n,\,nose}}{da_{n,\,cg}}$, percent	2.0	2.0
$\frac{da_n}{d\alpha}$, percent	2.0	2.0
P, sec	0.005	0.010
$T_{1/2}$, sec	0.01	0.02

TABLE V

CALCULATED ACCURACY OF PARAMETERS

[Increments may be positive or negative]

Increments in parameters due to probable errors in the quantities	C_{L_α} for—		$C_{D,min}$ for—		$\frac{x_{ac}}{\bar{c}}$ for—		$C_{m_q}+C_{m_{\dot\alpha}}$, percent, for—		$C_{L,t}$ for—		C_m for—	
	$M=1.35$	$M=0.9$	$M=1.35$	$M=0.9$	$M=1.35$	$M=0.9$	$M=1.35$	$M=0.9$	$M=1.35$	$M=0.9$	$M=1.35$	$M=0.9$
W	0.0005	0.0005	0.0004	0.0002	0.004	0.002	------	------	$0.01C_{L,t}$	$0.01C_{L,t}$	-------	-------
q	.0019	.0045	.0015	.0018	------	------	3	11	$.03C_{L,t}$	$.06C_{L,t}$	-------	-------
Center of gravity	------	------	------	------	.005	.005	------	------	--------	--------	-------	-------
I_Y	------	------	------	------	.010	.005	2	2	--------	--------	$0.02C_m$	$0.02C_m$
a_n	------	------	------	------	------	------	------	------	.01	.02	.006	.012
a_l for unswept wing	------	------	.0076	.0144	------	------	------	------	--------	--------	-------	-------
a_l for all others	------	------	.0019	.0036	------	------	------	------	--------	--------	-------	-------
$\frac{da_{n,\,nose}}{da_{n,\,cg}}$	------	------	------	------	------	------	------	------	--------	--------	$.02C_m$	$.03C_m$
$\frac{da_n}{d\alpha}$	.0015	.0015	------	------	.010	.005	5	7	--------	--------	-------	-------
P	------	------	------	------	.030	.020	------	------	--------	--------	-------	-------
$T_{1/2}$	------	------	------	------	------	------	10	23	--------	--------	-------	-------
Root-mean-square error	.0025	.0048	.0078 / .0025	.0145 / .0040	.034	.022	12	26	[a].033	[a].064	[b].0066	[b].0125

[a] For $C_{L,t}=1.0$
[b] For $C_m=0.1$

was greater as the lift increased. This type variation of $d\epsilon/d\alpha$ with C_L is indicated by the data in reference 14. The exposed-wing lift-curve slope (fig. 27 (a)) indicated only a small amount of nonlinearity over the lift range covered and supports the foregoing statement concerning the downwash variation. Estimates of the exposed-wing lift-curve slope at supersonic speeds from the approximate linearized theory of reference 15 indicate very good agreement with the measured values.

The lift-curve slopes for the two swept-wing models in figure 27 (b) illustrate the usefulness of the rocket-propelled-model test technique for the investigation of aeroelasticity. The variation of lift-curve slope with Mach number is shown in figure 27 (b) for the exposed wings and complete models. The slopes are taken near a lift coefficient of 0.30 since data were available at this lift coefficient for both horizontal-tail deflections. The duralumin-wing lift-curve slopes for the complete model and exposed wing increase rapidly from a Mach number of 0.92 to 0.95 and then gradually decrease as the Mach number increases. The steel-wing lift-curve slopes show the same variation with Mach number but, as would be expected, have higher values than for the more flexible duralumin wing. Also shown in figure 27 (b) is the lift-curve slope of the exposed rigid wing as obtained by the method described in the section entitled "Aeroelastic Analysis."

The lift data obtained from the unswept-wing configuration are given in figures 27 (c) and 28. The data in figure 27 (c) indicate some nonlinearity of the lift curves in the region from $M=0.75$ to $M=1.0$ as evidenced by the different slopes obtained for lift coefficients in the regions $C_L=0$ and 0.4. No values of C_{L_α} could be determined near $C_L=0$ at supersonic speeds because of the small amplitudes of oscillation following positive elevator deflections. The indications are that the nonlinearity disappears at Mach numbers above 1.0. Figure 28 presents a summary of the lift information obtained on the unswept-wing model. At subsonic Mach numbers the model reached very high positive angles of attack each time the control was deflected in the negative direction. An examination of the telemeter record of normal acceleration indicated the onset of a high-frequency oscillation of about 120 cycles per second, the wing first bending frequency. The value of lift coefficient where this oscillation began was taken to define the buffet boundary shown in figure 28. Beyond the buffet boundary the model apparently stalled. The points where this occurred are indicated by the maximum lift coefficient $C_{L,max}$. These maximum lift coefficients were obtained under dynamic conditions and are not necessarily the same as those obtained during static tests. The maximum rate of change of angle of attack in terms of the nondimensional factor $\dfrac{d\alpha}{dt}\dfrac{\bar{c}}{2V}$ was 4.9 radians at a Mach number of 0.83 and the results of reference 16 indicate that any dynamic effect would be negligible at this test condition.

Static stability.—The static stability characteristics of all models are given in figure 29 as the variation of aerodynamic-center position with Mach number.

Results for the delta-wing model were obtained from both
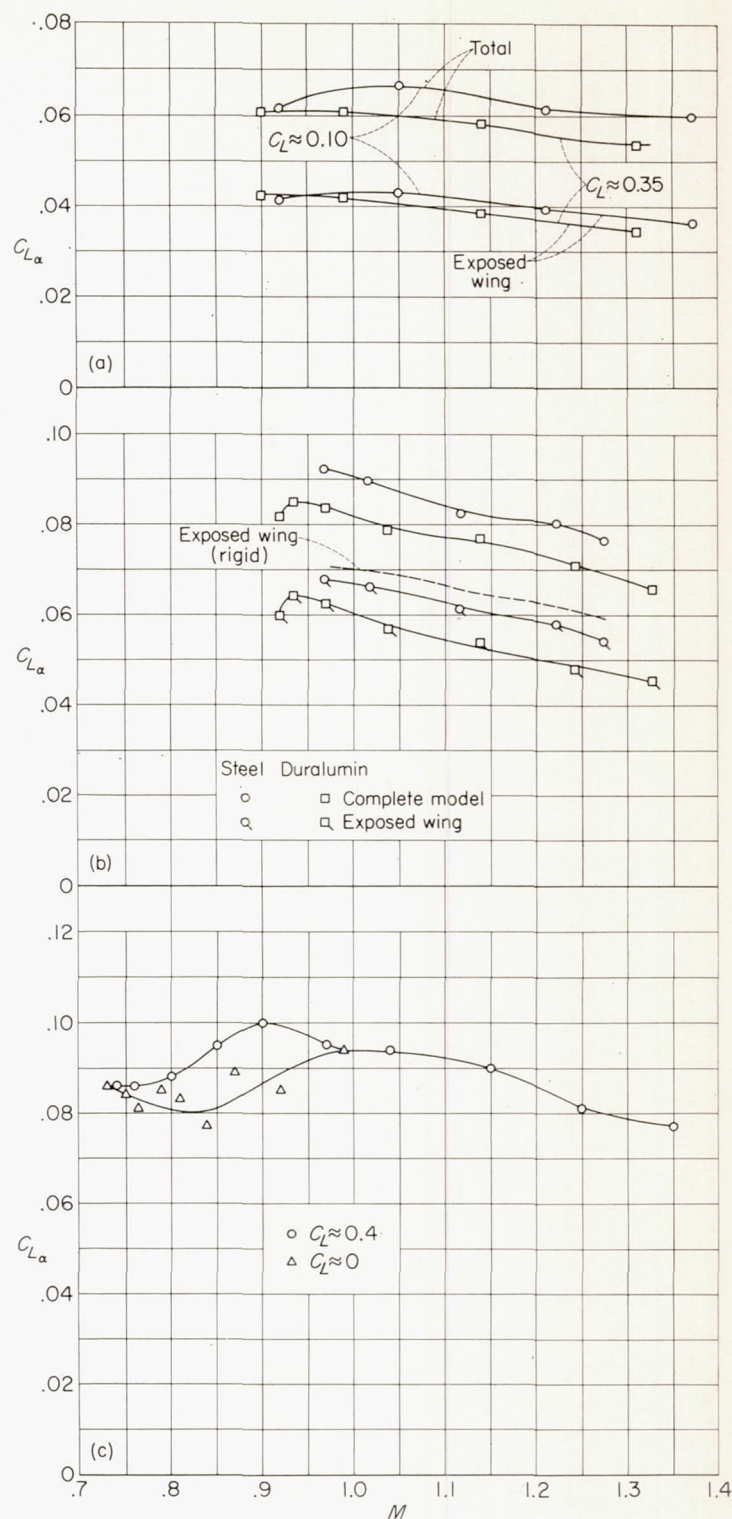
(a) Delta-wing model.
(b) Swept-wing models. $C_L \approx 0.30$.
(c) Unswept-wing model.

FIGURE 27.—Lift-curve slopes.

an analysis using the period of the oscillation and from two-accelerometer pitching-moment data; the agreement of the aerodynamic-center values determined from these two methods is very good. The fairly smooth variation of static stability with Mach number was similar to variations obtained from the tailless delta-wing configurations reported
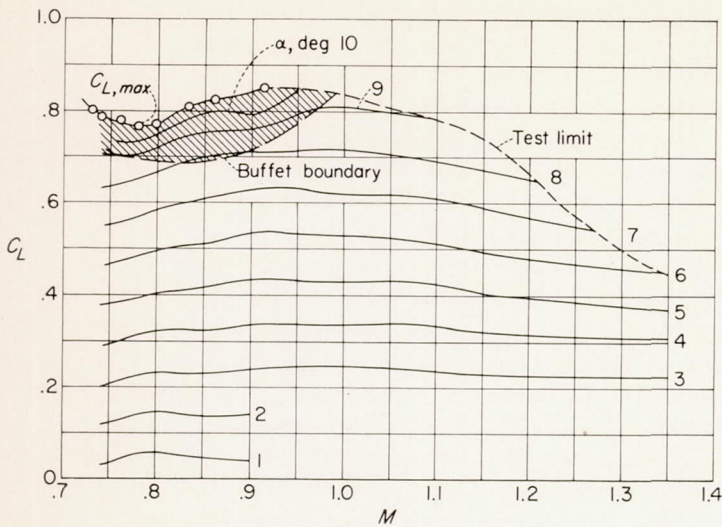
FIGURE 28.—Summary of buffet and maximum lift information. Unswept-wing model.

in reference 1. The stability decreased with increase in lift coefficient. It is believed that the primary factor contributing to the decrease in stability with increase in lift was an increase in $d\epsilon/d\alpha$ at the tail with an increase in lift. This increase was associated with the high tail position and was mentioned in the preceding section of this report as a possible cause of the reduction in total-lift-curve slope with an increase in lift coefficient.

The aerodynamic-center position for both swept-wing models is shown in figure 29 (b). The curves for both models were obtained by using the "period" method of analysis. The points for the steel-wing model were obtained from the double-differentiation method (eqs. (16) to (18)) and the points for the duralumin-wing model were obtained from the two-accelerometer method. With the exception of the one point at $M=1.27$ for the steel-wing model, the agreement between the points and the curve is good.

The aerodynamic-center position for the steel-wing model has the same variation with Mach number as the duralumin-wing model over the Mach number range 1.02 and 1.27. Over this Mach number range, however, the aerodynamic-center position is 3 to 6 percent more rearward than that for the steel-wing model. From the strip-theory method of the section entitled "Aeroelastic Analysis" the forward movement in aerodynamic-center position due to the inboard movement of the span load was calculated for the duralumin-wing model. A comparison between the calculation made for a 0.50-chord loading and the measured difference in aerodynamic-center position for the steel- and duralumin-wing models in figure 29 (b) shows that nearly all the loss in stability of the duralumin-wing model may be accounted for by the inboard movement of load on the wing.

The aerodynamic-center location for the unswept-wing configuration (fig. 29 (c)) indicates some nonlinearity in the pitching-moment curves at subsonic speeds. The curve faired through the data for $C_L=0.4$ at subsonic speeds has been dotted to indicate that the results were obtained from measuring periods during oscillations in which the angle-of-attack vane was against a stop during part of the oscillation.
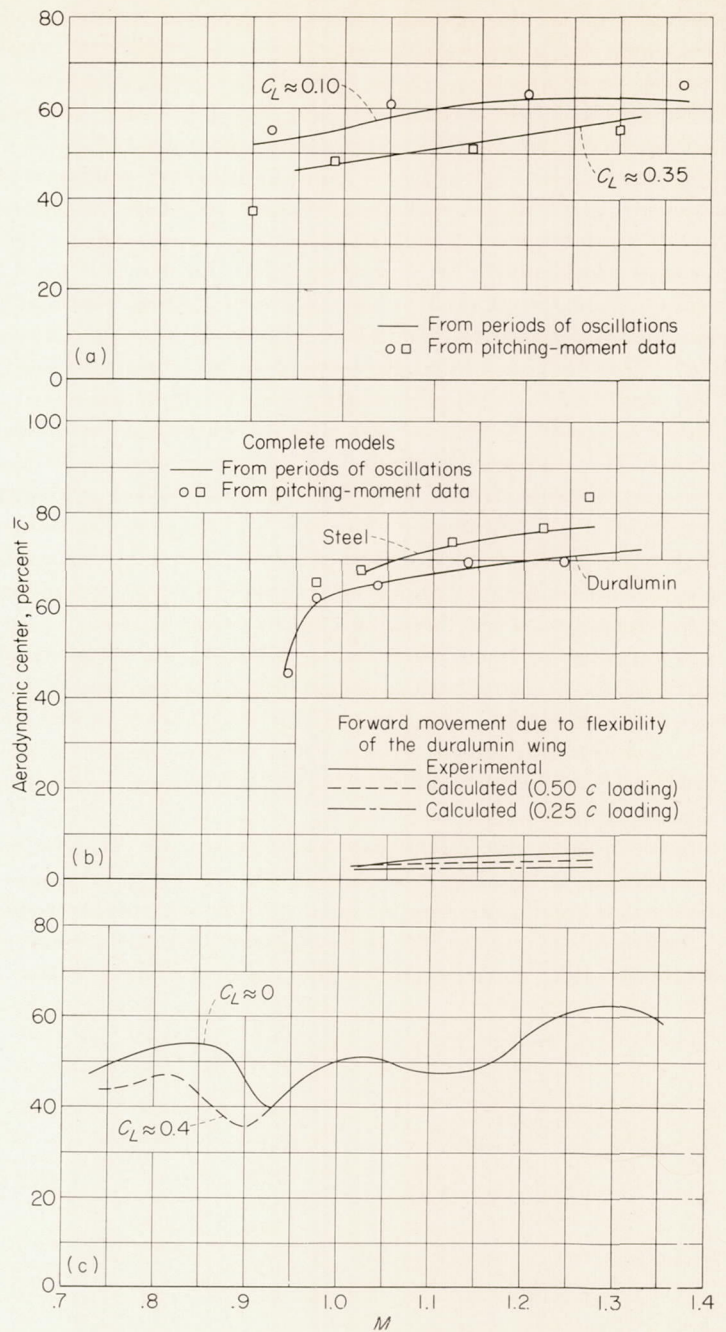
(a) Delta-wing model.
(b) Swept-wing models.
(c) Unswept-wing model.

FIGURE 29.—Aerodynamic-center locations.

As the Mach number is increased above about 0.82, the aerodynamic center first moves forward to its most forward location at 35 percent of the mean aerodynamic chord at a Mach number of 0.90. It then moves rearward at higher Mach numbers.

Damping in pitch.—The variation with Mach number of the damping-in-pitch parameter $C_{m_q}+C_{m_{\dot{\alpha}}}$ for all four models is shown in figures 22 and 30. These results were obtained from application of equation (31) by using the lift-curve-slope data of figure 27 along with the time to damp to one-half amplitude as discussed and illustrated previously.

For the delta-wing configuration an increase in the negative value of $C_{m_q}+C_{m_{\dot{\alpha}}}$ with increase in lift coefficient is indicated. (See fig. 22.) An increase in $d\epsilon/d\alpha$ with increase in lift coefficient mentioned previously could account for this increase in $C_{m_q}+C_{m_{\dot{\alpha}}}$ through its effect in increasing $C_{m_{\dot{\alpha}}}$.

The values of $C_{m_q}+C_{m_{\dot{\alpha}}}$ for both swept-wing models are shown in figure 30 (a). The duralumin-wing-model data are for a center-of-gravity position 20 percent of the mean aerodynamic chord more forward than that for the steel-wing model. This difference in center-of-gravity position was calculated to have a small effect on the damping-in-pitch derivative. The damping in pitch derivative for the duralumin-wing model shows a rapid variation with Mach number in the transonic speed range. This same variation might have occurred for the steel-wing model also, but damping data were not obtained for the steel-wing model below a Mach number of 1.0. The lower value of $C_{m_q}+C_{m_{\dot{\alpha}}}$ for the duralumin-wing model from Mach numbers 1.02 and 1.2 may not be due to aeroelasticity and is more likely to be an indication of the accuracy of the damping-in-pitch derivative.

The results for the unswept-wing configuration are given in figure 30 (b). These results indicate a large increase in the negative value of $C_{m_q}+C_{m_{\dot{\alpha}}}$ in the transonic range as was the case for the duralumin swept-wing model; however, the variation with Mach number after the peak is not as abrupt.

These results presented for $C_{m_q}+C_{m_{\dot{\alpha}}}$ indicate the wide range of numerical values associated with this parameter; this wide range makes it impossible to assess the dynamic stability of a configuration by means of this parameter alone.

Drag.—There are several ways of presenting the drag data obtained. The drag polars for the variation of C_D with C_L

were illustrated for the swept-wing configuration. (See fig. 15.) Figures 31 to 33 give the drag characteristics of all four models as a function of Mach number and illustrate some methods of plotting the results.

The drag data for the delta-wing configuration is given as the variation of drag coefficient with Mach number at several constant lift coefficients (fig. 31) and at two control deflections. Plots such as this give a rather complete picture of the drag characteristics of a configuration. For instance, the drag increment due to control deflection at lift coefficients of 0.2 and 0.3 is very evident. A large portion of this change in drag coefficient resulting from a change in tail incidence is the change in the streamwise component of the tail normal-force coefficient with change in tail incidence.

Another way of presenting drag data is illustrated by the results for the swept-wing configuration. The drag data for the steel- and duralumin-wing models of the swept-wing configuration are given in figure 32 as the variation of $C_{D,min}$ and $\dfrac{dC_D}{dC_L^2}$ with Mach number. The minimum drag values for the horizontal-tail setting of 0.14° for the steel-wing model and $-0.72°$ for the duralumin-wing model are in excellent agreement, the accuracy of the measurements and the small difference in horizontal-tail deflection being considered.
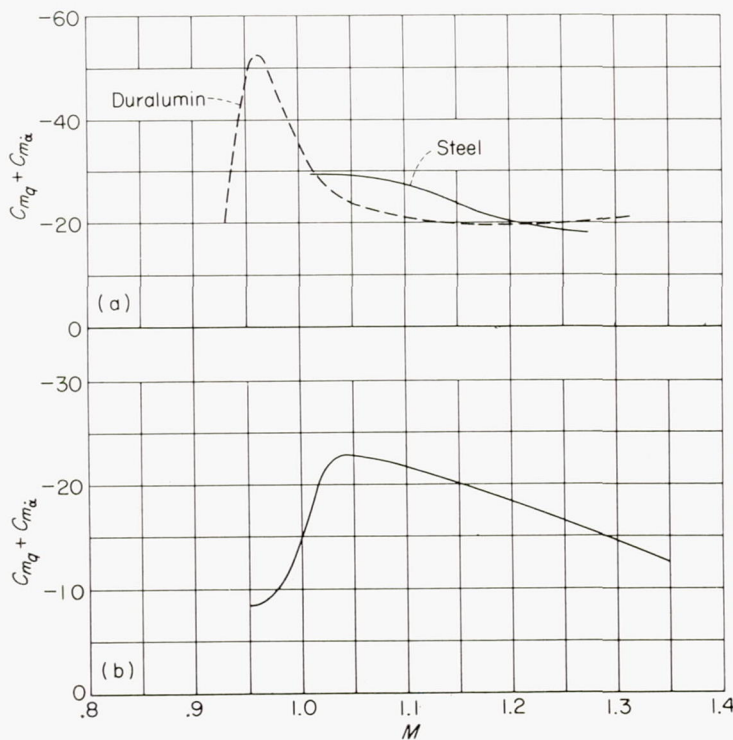
(a) Swept-wing models.
(b) Unswept-wing model.
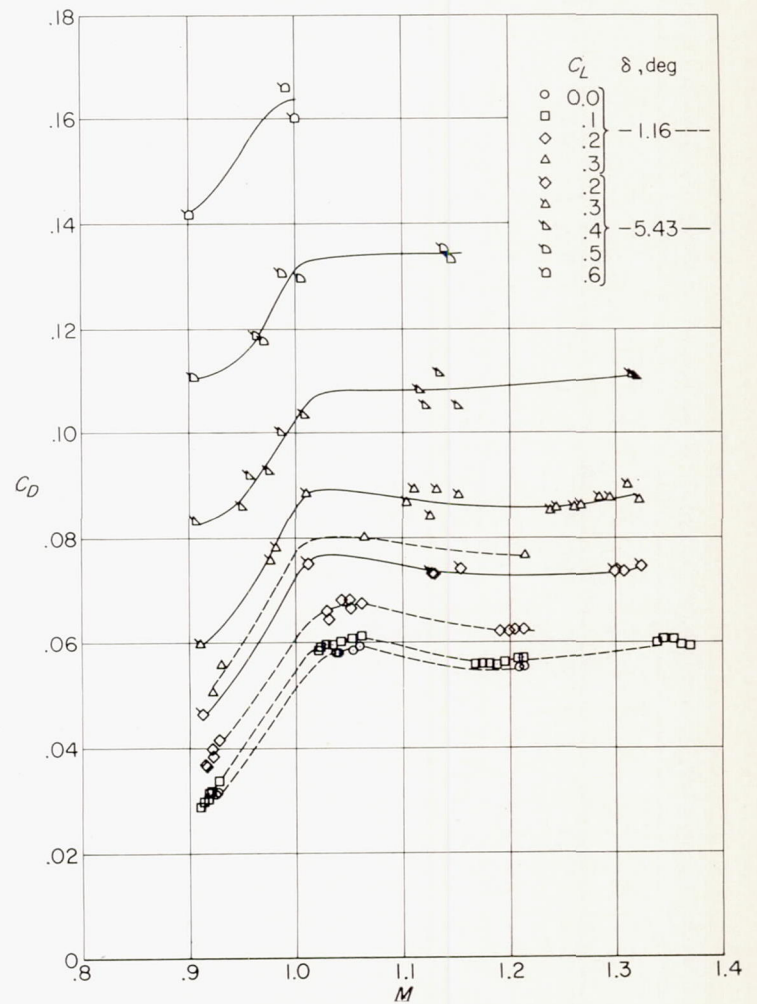FIGURE 30.—Pitching-moment damping factor.

FIGURE 31.—Variation of drag coefficient with Mach number and lift coefficient for the delta-wing model.

The drag due to lift of the models is presented in figure 32 (b) for lift coefficients of 0.50 and in figure 32 (c) for lift coefficients of 0.15 since the induced drag was found to be nonlinear with lift coefficient. Also shown in figures 32 (b) and 32 (c) are the ideal induced-drag factor $1/\pi A$ and the drag due to lift for no leading-edge suction $1/57.3\, C_{L_\alpha}$. For the $1/57.3\, C_{L_\alpha}$ comparison, the lift-curve slopes were measured near the trim lift coefficient corresponding to elevator deflections of $-3.0°$ and $0.14°$ for the steel-wing model and $-4.60°$ and $-0.72°$ for the duralumin-wing model. The lower induced drag for the duralumin-wing model suggests the possibility of a more efficient span loading for the flexible wing as a result of the inboard movement of the load when the wing deflects.

The results for the unswept-wing configuration are presented in figure 33. The longitudinal accelerometer in this model was calibrated to cover a sufficient range to include the accelerations during booster burning (about $18g$) and thus did not give very good accuracy on the accelerations (about $-1g$ to $-4g$) developed during the time the drag data were obtained. This is evidenced by the scatter of data in figure 33 (a). The minimum drag at supersonic speeds (fig. 33 (a)) is fairly high and is due mostly to the fuselage which is not a particularly good shape for supersonic speeds.

The effect of lift on drag is shown in various ways in figures 33 (b) and 33 (c). The $(L/D)_{max}$ (fig. 33 (b)) decreases by about one-half as the Mach number increases from 0.8 to 1.0. This decrease is apparently due to the increase in minimum drag because $\dfrac{dC_D}{dC_L^2}$ does not increase in this Mach
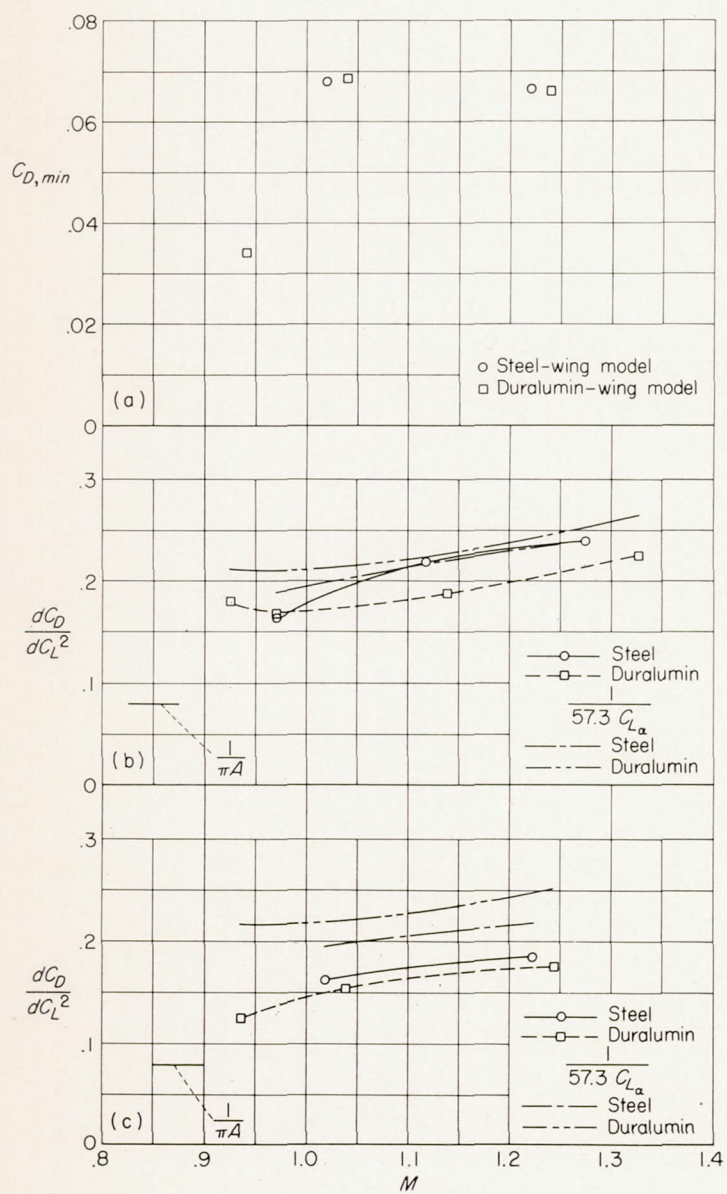
(a) Minimum drag.
(b) Drag due to lift $C_L \approx 0.50$.
(c) Drag due to lift $C_L \approx 0.15$.

FIGURE 32.—Drag characteristics of the swept-wing models.
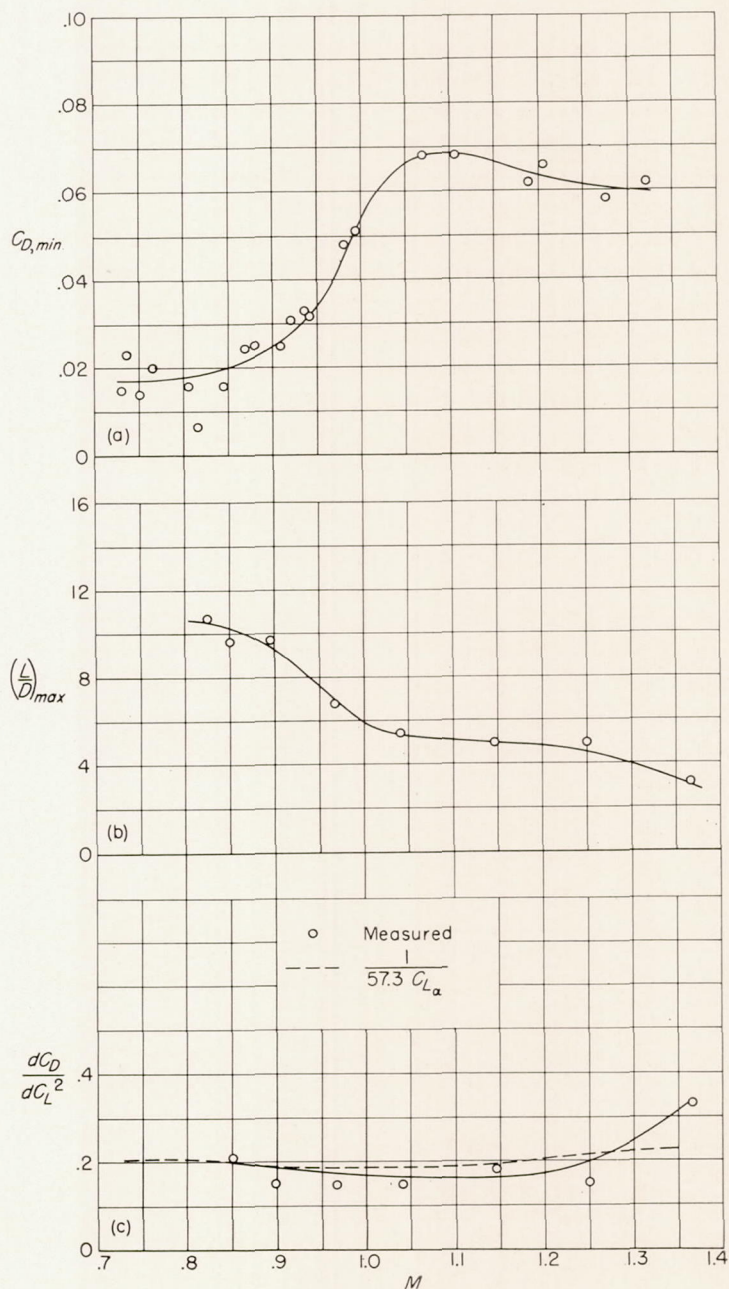
(a) Minimum drag.
(b) Maximum lift-drag ratio.
(c) Drag due to lift.

FIGURE 33.—Drag characteristics of the unswept-wing model.

number region, as shown in figure 33 (c). The dashed curve in figure 33 (c) is a plot of $\frac{1}{57.3 C_{L_\alpha}}$ which should equal the value of $\frac{dC_D}{dC_L^2}$ for a wing with the resultant force normal to the chord plane. The agreement between this curve and the measured values of $\frac{dC_D}{dC_L^2}$ is good except at the highest Mach numbers.

Control effectiveness.—The longitudinal control consisted of all-movable stabilizers which were the same on all models except that on two models the gaps at the roots were sealed as mentioned previously. When based on the same dimensions, the values of C_{m_δ} should thus be the same for all models except for the effect of the gaps. Figure 34 shows values of C_{m_δ} for the three configurations multiplied by $S\bar{c}/l_t$ in each case to furnish a common basis for comparison. The single curve shown for each configuration is the average of the values obtained by the methods illustrated previously. (See fig. 23 (a).) The cross-hatched area indicates the region which contained all the individual values of C_{m_δ} as determined by all the methods.

When the nonlinearity of the pitching-moment data discussed earlier is considered, the agreement of the data shown in figure 34 is believed to be reasonable since only two control deflections were available for each model and an assumption of linearity was thus required. Any effect of the gap at the horizontal-tail root on the control effectiveness is masked by the inaccuracy of determining C_{m_δ} for the models of this investigation.

APPLICATION TO FULL-SCALE AIRPLANES

When the aerodynamic characteristics have been determined from the model flight analysis, the performance and flying qualities of a similar full-scale airplane may, of course, be determined by substituting these quantities along with the airplane mass and geometric characteristics into the equations of motion. Certain questions of scaling arise when this procedure is used and some consideration has been given to this subject.
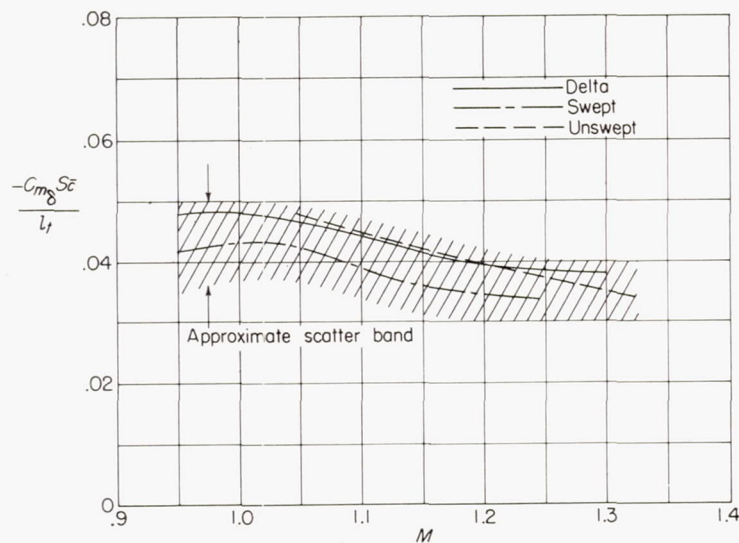
In the speed region under consideration, the Mach number is, of course, the most important similarity parameter and is used as the basic comparison variable. Viscous-flow effects are dependent upon Reynolds number and figure 35 shows the Reynolds numbers for the free-flight models and for two typical full-scale airplane flight conditions. The model Reynolds numbers approach those for airplanes at altitudes that are operationally feasible for these configurations and Mach numbers.

Experimental and theoretical analyses of unsteady aerodynamic effects indicate that these effects are dependent on the nondimensional frequency parameter $\frac{\omega\bar{c}}{2V}$. For the models discussed herein, the range of values of $\frac{\omega\bar{c}}{2V}$ was from 0.008 to 0.018. These values are considerably below the frequencies at which unsteady flow effects generally became appreciable and, in addition, are reasonably close to the probable values for full-scale airplanes of similar configuration.

The dynamics of the motion are affected by several similitude factors. If equation (33) for C_{m_α} is rewritten in terms of nondimensional quantities, the usually small damping term being neglected, the following expression for the nondimensional frequency parameter is obtained:

$$\frac{\omega\bar{c}}{2V} = \frac{1}{2\left(\frac{k_Y}{\bar{c}}\right)} \sqrt{\frac{-C_{m_\alpha}}{2\mu}} \tag{50}$$

FIGURE 34.—Comparison of control-effectiveness data. Average values used to determine curves.
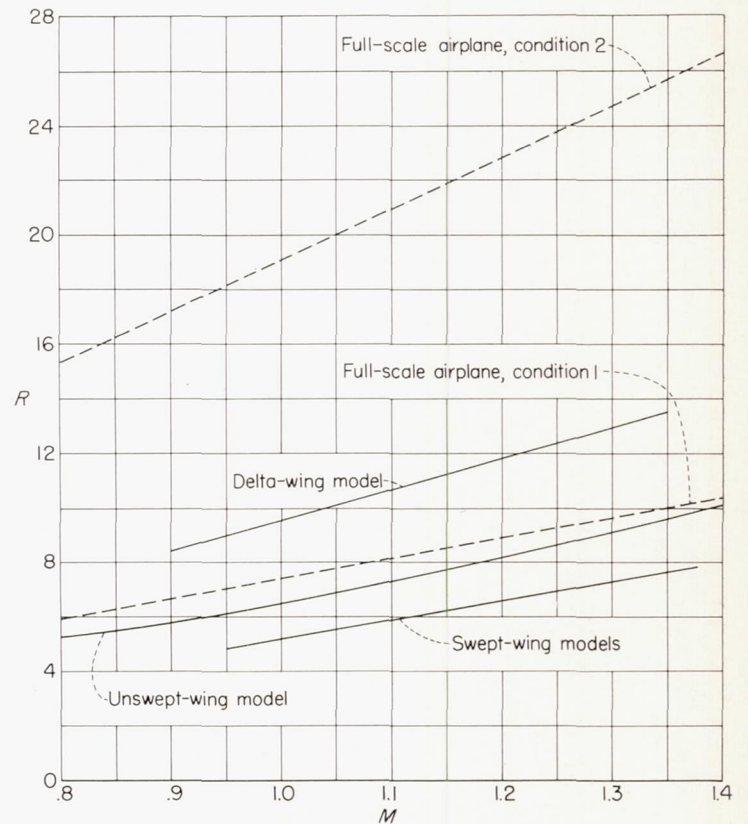

FIGURE 35.—Reynolds numbers based on mean aerodynamic chord for models and typical values for an airplane with $\bar{c}=10$ ft. Condition 1, 60,000 feet. Condition 2, 40,000 feet.

Values of the relative density factor μ for the models of the present investigation are shown in figure 36. Figure 36 also has an auxiliary scale that shows the equivalent altitude for an airplane with a chord of 10 feet and a wing loading of 100 pounds per square foot. It appears that the conditions under which the models were flown approximate those for typical airplanes at reasonable altitudes. A comparison of the values of $k_Y/\bar{c}$ for the present models and several current full-scale airplanes indicates that the values for the models are appreciably larger. This effect is at least partially compensated for in most cases by further forward locations of the center of gravity on the models, resulting in larger values of C_{m_α}. If dynamic similarity of the oscillation frequency only is desired, several factors are thus available for adjustment during test planning such as altitude, weight, radius of gyration, and center-of-gravity position.

The conditions governing the damping are more restrictive than those applying to the frequency. By making use of a nondimensional damping factor, such as the number of cycles required to damp to one-half amplitude, and deriving this factor from equations (26), (27), (29), and (50), the following expression can be obtained:

$$C_{1/2}=\frac{T_{1/2}}{P}=\frac{0.312\sqrt{-C_{m_\alpha}\mu}}{C_{L_\alpha}\dfrac{k_Y}{\bar{c}}-\dfrac{C_{m_q}+C_{m_{\dot{\alpha}}}}{2\left(\dfrac{k_Y}{\bar{c}}\right)}} \qquad (51)$$

Equation (51) shows that $k_Y/\bar{c}$ must be the same for the model and the full-scale airplane in order for the proportions of the damping contributed by the C_{L_α} and $C_{m_q}+C_{m_{\dot{\alpha}}}$ to be the same. The larger values of $k_Y/\bar{c}$ generally occurring on the models, as mentioned previously, results in a larger contribution of the C_{L_α}-term to the damping as compared with typical full-scale conditions. This condition has a dis-

advantage, in one sense, because the accuracy of determining $C_{m_q}+C_{m_{\dot{\alpha}}}$ is correspondingly decreased in the model tests. An important advantage from this increased effect of C_{L_α} may exist in some cases, however, because damped model motions may be obtained to permit determination of unstable values of $C_{m_q}+C_{m_{\dot{\alpha}}}$ which could lead to dynamic instability under full-scale conditions.

In general terms, it can be stated that the motions obtained on the models can be taken as applying to a full-scale airplane having the same center-of-gravity position, relative density, and nondimensional radius of gyration. The time histories of such motions may be applied directly to full-scale conditions if the time scale of the motions is multiplied by the ratio of the airplane size to the model size and the ratio of speed of sound at model altitude to speed of sound at airplane altitude and if the scale of angular velocities is reduced by the same factor. The latter statement applies to nonlinear motions as well as linear motions and also applies to combined pitching, rolling, and yawing motions if all the nondimensional radii of gyration are the same on the model and the full-scale airplane.

A further factor that needs to be considered is the scaling of aeroelastic effects. The parameter $qS(\theta/L)_{ref}$ utilized in figure 25 to relate data from different stiffness wings is one scaling factor that may be used. The range of the static-pressure ratio obtained on all models of this report is given in figure 37 and values of (θ/L) for the duralumin swept wing are given in figure 10. Because of the low altitude and resulting high dynamic pressures of the model test, the aeroelastic effects observed on the solid duralumin wing are directly applicable to an airplane with a more flexible wing at a higher altitude.

In case the model results are not directly applicable to the full-scale airplane, it is possible to correct the model results to rigid conditions, as illustrated herein, and then to use these results with the airplane elastic characteristics to determine the effects of flexibility on the airplane.

CONCLUDING REMARKS

A method has been set forth in some detail for determining aerodynamic performance and longitudinal stability parameters from free-flight tests of rocket-propelled models. The feasibility of the method has been demonstrated by data measured through the transonic speed range on several airplane configurations. The data are obtained from analysis of the model motions following control-surface disturbances. Data can be obtained over a considerable Mach number range during each flight.
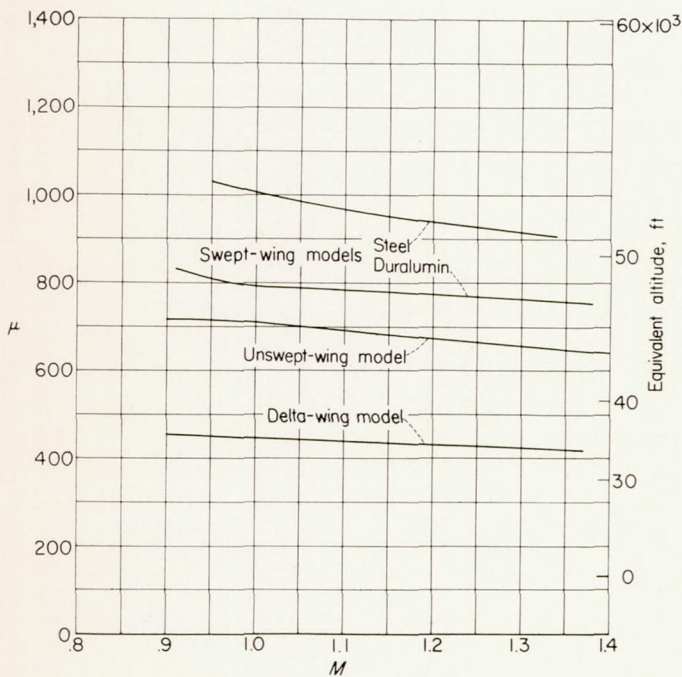

FIGURE 36.—Relative density factors for models and equivalent values of altitude for an airplane with $\bar{c}=10$ ft and $W/S=100$ lb/sq ft.
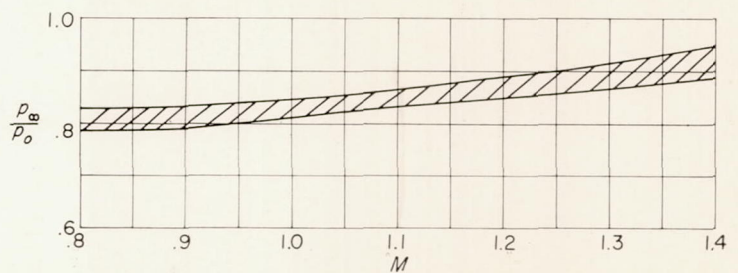

FIGURE 37.—Static-pressure ratio for all models.

The method makes use of accelerometers and an angle-of-attack indicator to permit instantaneous measurements of lift, drag, and pitching moments. Thus, nonlinear characteristics can be studied. For configurations which do not exhibit excessive lateral motions at high angles of attack, the maximum lift and buffeting characteristics may be determined. Effects of aeroelasticity may be readily obtained. Additional information can be obtained by analysis of the characteristics of the short-period free oscillations resulting from rapid control-surface deflections, but this procedure requires the assumption of linearity of the aerodynamic quantities during each oscillation. Some measure of nonlinearities may be obtained with the latter method, however, by studying oscillations at different trim angles of attack. Although the models decelerated continuously during the data-gathering portions of the flight tests, the assumption of constant velocity for the analysis was shown to have negligible effects for the tests reported herein.

Comparison of measured and calculated effects of wing flexibility, making use of measured structural influence coefficients, showed very good agreement. Where comparisons were possible, the values of the aerodynamic parameters determined by different methods showed generally very good agreement. The flight conditions and dynamic similitude factors for the tests described herein provide reasonably close approximation to typical full-scale airplane conditions.

LANGLEY AERONAUTICAL LABORATORY,
   NATIONAL ADVISORY COMMITTEE FOR AERONAUTICS,
   LANGLEY FIELD, VA., *August 19, 1957.*

REFERENCES

1. Mitcham, Grady L., Stevens, Joseph E., and Norris, Harry P.: Aerodynamic Characteristics and Flying Qualities of a Tailless Triangular-Wing Airplane Configuration As Obtained From Flights of Rocket-Propelled Models at Transonic and Low Supersonic Speeds. NACA TN 3753, 1956. (Supersedes NACA RM L9L07.)

2. Gillis, Clarence L., Peck, Robert F., and Vitale, A. James: Preliminary Results From a Free-Flight Investigation at Transonic and Supersonic Speeds of the Longitudinal Stability and Control Characteristics of an Airplane Configuration With a Thin Straight Wing of Aspect Ratio 3. NACA RM L9K25a, 1950.

3. Peck, Robert F., and Mitchell, Jesse L.: Rocket-Model Investigation of Longitudinal Stability and Drag Characteristics of an Airplane Configuration Having a 60° Delta Wing and a High Unswept Horizontal Tail. NACA RM L52K04a, 1953.

4. Vitale, A. James: Effects of Wing Elasticity on the Aerodynamic Characteristics of an Airplane Configuration Having 45° Swept-back Wings As Obtained From Free-Flight Rocket-Model Tests at Transonic Speeds. NACA RM L52L30, 1953.

5. Mitchell, Jesse L., and Peck, Robert F.: An NACA Vane-Type Angle-of-Attack Indicator for Use at Subsonic and Supersonic Speeds. NACA TN 3441, 1955. (Supersedes NACA RM L9F28a.)

6. Harris, Orville R.: Determination of the Rate of Roll of Pilotless Aircraft Research Models by Means of Polarized Radio Waves. NACA TN 2023, 1950.

7. Shinbrot, Marvin: On the Analysis of Linear and Nonlinear Dynamical Systems From Transient-Response Data. NACA TN 3288, 1954.

8. Triplett, William C., Brown, Stuart C., and Smith, G. Allan: The Dynamic-Response Characteristics of a 35° Swept-Wing Airplane As Determined From Flight Measurements. NACA Rep. 1250, 1955. (Supersedes NACA RM A51G27 by Triplett and Smith and NACA RM A52I17 by Triplett and Brown.)

9. Hoch, H.: Untersuchungen zur Stabilität der leitstrahlgeführten Flakrakete. FB Nr. 1892/3 Deutsche Luftfahrtforschung (Berlin-Adlershof), 1944.

10. Oswald, Telford W.: Dynamic Behavior During Accelerated Flight With Particular Application to Missile Launching. Jour. Aero. Sci., vol. 23, no. 8, Aug. 1956, pp. 781–791.

11. Gardner, C. S., and Ludloff, H. F.: Influence of Acceleration on Aerodynamic Characteristics of Thin Wings in Supersonic and Transonic Flight. Preprint No. 186, Inst. Aero. Sci., Inc., Jan. 1949.

12. Parks, James H., and Kehlet, Alan B.: Longitudinal Stability, Trim, and Drag Characteristics of a Rocket-Propelled Model of an Airplane Configuration Having a 45° Sweptback Wing and an Unswept Horizontal Tail. NACA RM L52F05, 1952.

13. Eshback, Ovid W., ed.: Handbook of Engineering Fundamentals. John Wiley & Sons, Inc., 1936, pp. 2–127.

14. Allen, Edwin C.: Investigation of a Triangular Wing in Conjunction With a Fuselage and Horizontal Tail To Determine Downwash and Longitudinal-Stability Characteristics—Transonic Bump Method. NACA RM A51F12a, 1951.

15. Morikawa, George.: Supersonic Wing-Body Lift. Jour. Aero. Sci., vol. 18, no. 4, Apr. 1951, pp. 217–228.

16. Harper, Paul W., and Flanigan, Roy E.: The Effect of Rate of Change of Angle of Attack on the Maximum Lift of a Small Model. NACA TN 2061, 1950.